INL/EXT-18-51460

Light Water Reactor Sustainability Program

Uncertainty Quantification in Vibro-Acoustics Diagnosis of Alkali-Silica Reaction Degradation in Medium-Sized Concrete Samples

September 2018

U.S. Department of Energy

Office of Nuclear Energy

INL/EXT-18-51460

Light Water Reactor Sustainability Program

Uncertainty Quantification in Vibro-Acoustics Diagnosis of Alkali-Silica Reaction Degradation in Medium-Sized Concrete Samples

Sankaran Mahadevan
Sarah Miele
Pranav Karve
Julia Finfrock
Garrett Thorne
Vivek Agarwal
Eric Giannini

September 2018

Idaho National Laboratory
Idaho Falls, Idaho 83415

Vanderbilt University
Nashville, Tennessee 37235

Prepared for the
U.S. Department of Energy
Office of Nuclear Energy
Under DOE Idaho Operations Office
Contract DE-AC07-05ID14517

ABSTRACT

The objectives of this ongoing research project focus on health monitoring and data analytics of concrete slabs with alkali-silica reaction (ASR) degradation. Researchers at Vanderbilt University cast a controlled concrete slab with four pockets of reactive aggregates (pure silica, wells, placitas, and spratt) and cured in representative conditions to accelerate degradation due to ASR. A set of four concrete samples were also cast and cured at the University of Alabama for ASR testing. Of these four samples, two slabs contained reactive aggregates while the other two had the non-reactive aggregate counterparts mixed throughout the samples. Vibro-acoustic testing was used on these slabs to locate ASR damage within the reactive samples.

Vibro-acoustic modulation (VAM) is a vibration-based nondestructive examination (NDE) method that utilizes signatures of nonlinear dynamic interactions on contact surfaces of crack or delamination damage to detect and localize the damage. VAM analysis was conducted on both the Vanderbilt and Alabama samples using multiple variables for damage detection and localization. This report discusses in detail the results from the data analysis of the vibro-acoustic testing on concrete slabs cured at Vanderbilt University and the University of Alabama. Results for damage localization are dependent on multiple variables used in the vibro-acoustic modulation experiments. A major focus of this report is to quantify the uncertainty in the diagnosis due to multiple factors and uncertainty sources. Researchers applied the uncertainty quantification methodology presented in this report to VAM-based diagnosis and prognosis. However, the methodology is general, and is capable of being applied to multiple techniques that collect spatially distributed data. Future work needs to investigate the incorporation of uncertainty quantification in developing a robust Prognostics and Health Management framework.

Digital image correlation is a three-dimensional, full-field, optical NDE technique to measure contour, deformation, vibration, and strain. This report also discusses the application of the digital image correlation technique to study ASR-related degradation on a large concrete specimen at the University of Tennessee. Research observations are collected and presented in this report.

EXECUTIVE SUMMARY

One challenge facing the current fleet of light water reactors in the United States is age-related degradation of their passive assets, including concrete, cables, piping, and the reactor pressure vessel. As the current fleet of nuclear power plants (NPPs) continues to operate for 60 years or more, it is important to understand the current and the future condition of passive assets under different operating conditions that would support operational and maintenance decisions. To ensure safe and reliable long-term operation of the current fleet, the U.S. Department of Energy's Office of Nuclear Energy funds the Light Water Reactor Sustainability Program to develop the scientific basis for extending the operation of commercial light water reactors beyond the current license extension period.

In this project, researchers focused on NPP concrete structures rather than other passive assets. These reinforced concrete structures can be grouped into following categories: (1) primary containment; (2) containment internal structures; (3) secondary containments/reactor buildings; and (4) spent fuel pool and cooling towers.

These concrete structures are affected by a variety of degradation mechanisms that are related to chemical, physical, and mechanical causes, as well as to irradiation. Age-related degradation of concrete results in gradual microstructural changes (e.g., slow hydration, crystallization of amorphous constituents, and reactions between cement paste and aggregates). Structural health monitoring of concrete helps assess the current condition of a structure and provides high-confidence actionable information regarding structural integrity and reliability.

Vanderbilt University, in collaboration with Idaho National Laboratory and Oak Ridge National Laboratory, is developing a probabilistic framework for structural health monitoring and managing the condition of aging concrete structures in NPPs. This integrated framework includes four elements: (1) monitoring; (2) data analytics; (3) uncertainty quantification; and (4) prognosis.

This continuing research project collected degradation data for concrete structures from a series of experiments conducted under controlled laboratory conditions. Also being assessed is the ability of nondestructive examination (NDE) methods to characterize concrete deterioration and correlate it with structural performance.

This report focuses on concrete degradation caused by alkali-silica reaction (ASR). Concrete specimens were prepared to develop accelerated ASR degradation in a laboratory setting. NDE techniques, which include thermography, mechanical deformation measurements, nonlinear impact resonance-acoustic spectroscopy, and vibro-acoustic modulation (VAM), were previously used to detect the damage caused by ASR on concrete slabs cured at Vanderbilt University, and documented in an earlier report.

The objectives of this report were to examine the application of VAM and digital image correlation (DIC) techniques in ASR damage diagnosis and to develop approaches for uncertainty quantification in diagnosis. The VAM technique was applied to a 24 in. x 24 in. x 6 in. slab cast at Vanderbilt University with four pockets of reactive aggregates, and four 24 in. x 12 in. x 12 in. slabs with reactive and non-reactive aggregates (dispersed throughout the slabs). The DIC technique was applied to a large concrete mock-up at the University of Tennessee, Knoxville. The main outcomes of the experiments and subsequent analyses include:

1. VAM successfully detected and localized the damage in the medium-sized concrete slabs from both Vanderbilt and Alabama. The detection and locations of damage using VAM technique is dependent on the pumping and probing actuator locations, the two excitation amplitudes, and the two excitation frequencies.
2. The uncertainty quantification effort first developed a neural network surrogate model to speed up the forward and inverse problems in uncertainty quantification.

3. The neural network model is verified by comparison with the experimental data, and the observed agreement is moderate.
4. The neural network model is employed to quantify the uncertainty in the damage diagnosis, and the result is shown as probability of damage at each location.
5. The neural network is also employed for sensitivity analysis, thus quantifying the relative contributions of different experimental parameters on the uncertainty of the damage diagnosis.

The monitoring of the large specimen at the University of Tennessee is complete, and the DIC analysis results presented in this report cover the entire range of DIC data collected over the two-year period.

The uncertainty quantification methodology presented in this report was applied to VAM-based diagnosis and prognosis. However, the methodology is general and can be applied to multiple techniques that collect spatially distributed data. Future work needs to investigate the incorporation of uncertainty quantification in developing a robust Prognostics and Health Management framework.

ACKNOWLEDGMENTS

This report was made possible through funding by the U.S. Department of Energy's Light Water Reactor Sustainability Program. We are grateful to Alison Hahn of the U.S. Department of Energy and Bruce Hallbert and Craig A. Primer at Idaho National Laboratory for championing this effort. We also thank Jodi Vollmer and Katie S. Stokes at Idaho National Laboratory for technical editing and formatting of the report.

CONTENTS

FIGURES

TABLES

ACRONYMS

ASR	alkali-silica reaction
DIC	digital image correlation
EPRI	Electric Power Research Institute
FFT	Fast Fourier Transform
LS	linear spectrum
NaOH	sodium hydroxide
NDE	nondestructive examination
NIRAS	nonlinear impact resonance-acoustic spectroscopy
NPP	nuclear power plant
PSD	power spectral density
PHM	Prognostics and Health Management
SBSum	sideband sum
SHM	structural health monitoring
VAM	vibro-acoustic modulation

Uncertainty Quantification in Vibro-Acoustics Diagnosis of Alkali-Silica Reaction Degradation in Medium-Sized Concrete Samples

1. INTRODUCTION

The majority of existing nuclear power plants (NPPs) continue to operate beyond their initial licensed life expectancy. As NPPs continue to operate, their passive structures, systems, and components suffer deterioration that affects structural integrity and performance. Monitoring the condition of these elements of an NPP is essential for ensuring that their conditions meet performance and safety requirements over the entire expected plant lifespan.

This project focuses on concrete structures in NPPs. The concrete structures are grouped into the following categories: (1) primary containment; (2) containment internal structures; (3) secondary containment/reactor buildings; and (4) other structures such as used fuel pools, dry storage casks, and cooling towers. These concrete structures are affected by a variety of chemical, physical, and mechanical degradation mechanisms, such as alkali-silica reaction (ASR), chloride penetration, sulfate attack, carbonation, freeze-thaw cycles, shrinkage, and mechanical loading (Naus 2007). The age-related deterioration of concrete results in continuing microstructural changes (e.g., slow hydration, crystallization of amorphous constituents, and reactions between cement paste and aggregates). Therefore, it is important that changes to these passive structures and systems are measured and monitored over long periods of time. Researchers must analyze impacts on the integrity of the components to support long-term operations and maintenance decisions of existing fleet of nuclear reactors.

Structural health monitoring (SHM) can produce actionable information regarding structural integrity. When conveyed to the decision-maker, the information enables risk management with respect to structural integrity and performance. The SHM methods and technologies include assessment of critical measurements, monitoring, and analysis of aging concrete structures under different operating conditions. In addition to data from the specific system being monitored, information may also be available for similar or nominally identical systems in an operational NPP fleet, as well as legacy systems. Therefore, to take advantage of this valuable information Christensen (1990) suggested that assessment and management of aging concrete structures in NPPs requires a more systematic and dynamic approach than simple reliance on existing code margins of safety.

Through the Light Water Reactor Sustainability Program, national laboratories (Idaho National Laboratory and Oak Ridge National Laboratory) and universities (Vanderbilt University, University of Nebraska-Lincoln, University of Alabama, University of South Carolina, and Georgia Tech University) have begun research on concrete SHM techniques. The focus in this report is on the collaboration between national laboratories and Vanderbilt University in researching concrete SHM in accordance with the proposed framework discussed in Mahadevan et al. (2014).

The goal of this research is to enable plant operators to make risk-informed decisions on structural integrity, remaining useful life, and performance of concrete structures across the NPP fleet. The long-term research objective of this project is to produce actionable information regarding structural integrity that is individualized for a structure of interest and its performance goals. In addition, the project supports the research objectives of three pathways under the Light Water Reactor Sustainability Program (i.e., the Advanced Information, Instrumentation, and Control Systems Technologies Pathway; the Materials Aging and Degradation Pathway; and the Risk-Informed Safety Margin Characterization Pathway).

Vanderbilt University, in collaboration with Idaho National Laboratory and Oak Ridge National Laboratory, is developing a framework for evaluating and forecasting the health of aging NPP concrete structures that are subject to physical, chemical, and mechanical degradation (Mahadevan et al. 2014; Agarwal and Mahadevan 2014). The framework will investigate concrete structure degradation by integrating the following technical elements: (1) health condition monitoring; (2) data analytics; (3) uncertainty quantification; and (4) prognosis. For details on each element of the proposed framework, refer to Mahadevan et al. (2014). The framework will help plant operators to make risk-informed decisions on structural integrity, remaining useful life, and concrete structure performance. The demonstration performed at Vanderbilt University using various techniques to assess ASR degradation in controlled concrete specimens was reported in Mahadevan et al. (2016, 2017).

The objective of this report is to examine the use of vibro-acoustic modulation (VAM) in informing the PHM framework. A series of experiments were conducted at the Vanderbilt University to provide sufficient degradation data in support of the PHM framework (Mahadevan et al. 2014; Mahadevan et al. 2016) used to examine and forecast the condition of aging concrete structures in NPPs. Within this experimental campaign, multiple concrete slab samples are exposed to different accelerated aging conditions in a laboratory to ensure formation of ASR gel within an observable time frame. These concrete samples also differ in sizes and types of embedded aggregates. The above-mentioned VAM is used to detect and assess the ASR-induced damage in these concrete samples over an extended period of time.

The technical background, experimental setting, data processing, significant results, technical findings, and conclusion are included in the remainder of the report is organized as follows:

- Section 2 discusses the technical basics of the ASR development and the VAM and DIC techniques used to assess the effects of ASR on the integrity of concrete samples developed at Vanderbilt University.
- Section 3 describes the various concrete specimens exposed to different ASR accelerated degradation conditions and the laboratory experimental setup of the VAM and DIC techniques.
- Section 4 presents data analysis methods applied to the collected monitoring data and significant technical findings.
- Section **Error! Reference source not found.** discusses uncertainty quantification of ASR damage diagnosis using VAM test results.
- Section 6 describes the application of DIC technique to the large concrete slab cast at the University of Tennessee, Knoxville.
- Section 7 discusses the research summary and future work.

2. TECHNICAL BACKGROUND

2.1 Alkali-Silica Reaction Development and Impact

The ASR is a reaction in concrete between the alkali hydroxides (K^+ and Na^+) in the pore solution and the reactive non-crystalline (amorphous) silica (S^{2+}) found in many common aggregates, given sufficient moisture. This reaction occurs over time and causes the expansion of the altered aggregate by the formation of a swelling gel of calcium silicate hydrate (C-S-H). Reactive silica is mainly provided by reactive aggregates and the alkalis by the cement clinker. ASR swelling results from the relative volume increase between the product and reactant phases involved in the chemical reaction. First, the products expand in pores and micro-cracks of the cementitious matrix. Once this free expansion space is filled, the swelling is restrained, and the product phases exert local pressure on the surrounding concrete skeleton (Ulm 2000). Figure 1 depicts the mechanism of ASR (Kreitman 2011).

With the presence of water, the ASR gel increases in volume and exerts an expansive pressure inside the material, causing spalling micro-to macro-cracks (due to nonhomogeneous swelling related to non-uniform

moisture distribution). As a result, ASR reduces the stiffness and tensile strength of concrete, because these properties are particularly sensitive to micro-cracking. ASR also can cause serious cracking in concrete, resulting in critical structural problems that can even force the demolition of a particular structure. The serviceability of concrete structures includes the resistance to excessive deflections, as well as a host of other durability concerns that can shorten the service life of a structure. Large surface crack widths and deep penetration of open surface cracks promote ingress moisture and any dissolved aggressive agents, such as chlorides. Additionally, of concern for concrete deflection capabilities is loss of concrete stiffness and potential for reinforcement yield.

ASR is a complex chemical phenomenon, the rate and extent of which depend on a number of material and environmental parameters, for which the interactions among parameters is not fully understood. This critical nature of ASR on premature concrete deterioration requires the quantitative assessment of ASR structural effects during service life (both in time and space). In particular, a combined experimental modeling investigation method is required to evaluate the impact of ASR on the dimensional stability of concrete structures. Although ASR has been identified as a cause of deterioration of numerous concrete structures and research has yielded some understanding of the mechanism of the reaction, the structural effects of ASR and how to best assess the extent of damage to existing structures remain major topics of ongoing research. This is because the expansion and cracking patterns (the most obvious sign of distress) caused by ASR affect both the concrete and the reinforcing steel, but similar crack patterns can also be produced by other distress mechanisms (i.e., drying shrinkage and sulfate attack).

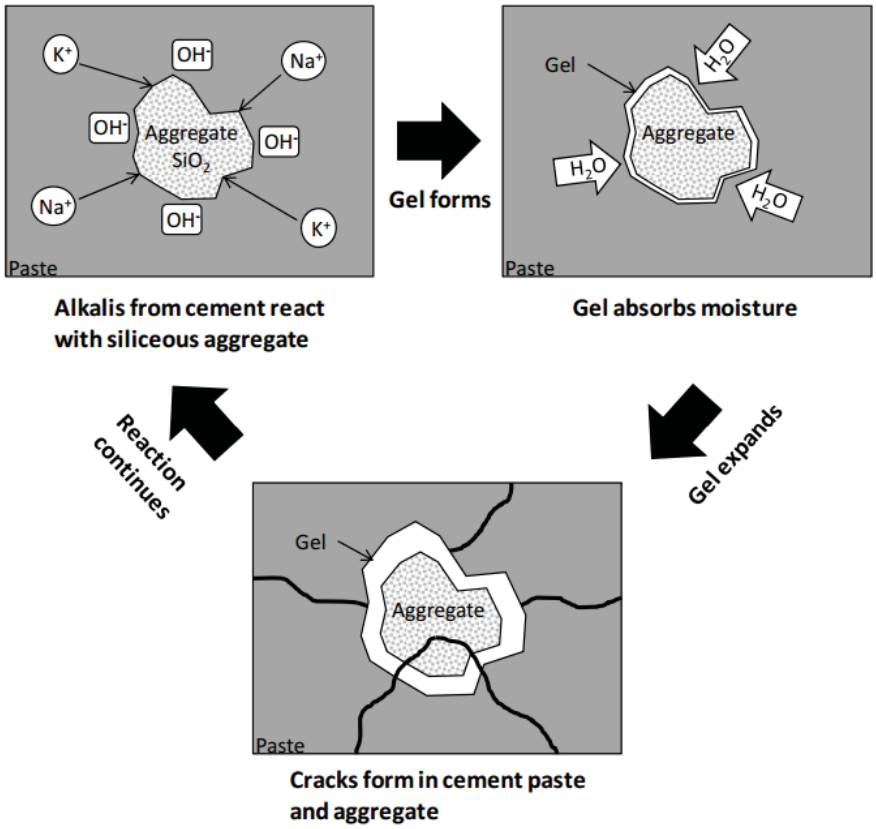

Figure 1: Mechanism of ASR (Kreitman 2011).

In the nuclear industry, a scoping study of ASR in concrete is performed to support future activities that include evaluating the effects of ASR on the structural capacity. From a safety perspective, the remaining capacity of a structure exhibiting distress due to ASR is an important factor in operational and maintenance management decisions. This is a challenging task for various reasons. First, the extent of the degradation will vary throughout the element as a function of the moisture content and as a function of the

degree of restraint provided by the steel reinforcement. Also, it may be difficult to predict the properties of the concrete using certain testing results taken from the structure. The size of the defects caused by the ASR may be large compared to a small structure, such as the cylinder (resulting in anomalously low tested strength), but the defects are small compared to the larger structure (suggesting there may be sufficient capacity). In addition, there is no reliable nondestructive means of estimating the degree of the reaction in an existing concrete structure.

ASR can potentially affect concrete properties and performance characteristics, such as compressive strength, the modulus of elasticity, flexural stiffness, shear strength, and tensile strength (Agarwal et al. 2015). ASR can also impact material properties, but the structural performance of concrete elements depends on whether or not the concrete is unconfined or confined within reinforcing bars. The concrete core testing was conducted at the Seabrook Station Nuclear Power Plant in February 2011 as part of the license renewal submission (NextEra Energy Seabrook 2012). These tests confirmed the presence of ASR-induced cracks in various structures within the plant and reduced modulus to some extent. Researchers evaluated the impact of reduced modulus on ASR-affected structures. This evaluation found that the overall structure integrity was still within the strength requirements.

2.2 Damage Evaluation Techniques for Monitoring Alkali-Silica Reaction

Researchers have studied multiple types of SHM techniques, broadly categorized as contact monitoring techniques and non-contact monitoring techniques, for detecting ASR damage in concrete structures. The contact monitoring techniques include mechanical deformation measurement, acoustic emission, ultrasonic detection, nonlinear impact resonance-acoustic spectroscopy, VAM, and diffuse wave spectroscopy. The non-contact monitoring techniques include DIC and infra-red thermography imaging. The standard test methods for determining the potential alkali-silica reactivity and for determination of the amount of time needed for concrete to change due to ASR are documented in ASTM C1567-13 and ASTM C1293-08b, respectively. Earlier reports by Mahadevan et al. (2016, 2017) have studied various techniques and found them to be useful in damage detection. The VAM technique, investigated in detail in this report, shows particular promise in damage localization. In addition, the DIC technique is investigated in detail with respect to the large sample at University of Tennessee, Knoxville (UTK). Below is a brief overview of the VAM and DIC techniques.

2.2.1 Vibro-Acoustic Modulation

Vibro-acoustic modulation (VAM), also known as nonlinear wave modulation spectroscopy, is a NDE technique that relies on detecting dynamic signature of nonlinear structural behavior as the primary indicator of damage. Specifically, VAM aims at detection of modulation of a higher frequency by a lower frequency caused by delamination or cracks in structural components. Researchers have demonstrated in the past the utility of VAM for detecting debonding flaws and cracks in composites, metals, as well as ASR-induced cracks in concrete (Chen et al. 2008; Chen et al. 2009).

In a VAM technique, the structural component of interest is excited simultaneously using a combination of two signals of specific frequencies, and the dynamic response is measured at various locations using acoustic sensors (accelerometers). The low-frequency input is termed the “pump,” and the high-frequency input is termed the “probe” (Kim et al. 2014). The geometric or material nonlinearity in the form of variable contact area or nonlinear adhesive bond at the surfaces of a crack or a delamination causes modulation of the probing frequency (f_{pr}) by the pumping frequency (f_{pu}). This modulation, and hence the presence of the flaw, can be seen in the frequency spectra of measured response as peaks of higher magnitude (sidebands) around the probe frequency.

Researchers used the interaction of these signals at different frequencies to understand the nonlinear stress-strain relationship in the structure of interest. For example, Figure 2 shows the response when the two excitation signals are theoretically applied to a structure. If the structure is linear and damped, the

response in the steady state is the linear superposition of the responses of each signal, and only the linear components of Figure 2 will appear in the frequency spectrum of the response.

Damage in a structure introduces nonlinearity and as a result, the response contains both the probing frequency and the pumping frequency in addition to other frequency components such as harmonics of each signal and sidebands around the probing signal as shown in Figure 2. Most of the previous work on VAM-tests has focused on *detection* of damage based on the presence of side bands in the spectrum of dynamics response of the structure. Recently, Singh et al. (Singh et al. 2017) showed that a VAM test can be used for damage *localization* or damage mapping. They hypothesized that the effect of (geometric or material) nonlinearities is pronounced near the location of the flaw, and hereafter, the relative magnitude of a sidebands-based damage index may enable localization of the flaw. That is, if the spatial distribution showing the variation of the damage index is obtained using a sensor grid, the damage is located in the neighborhood of sensors exhibiting higher magnitude of the damage index.

They tested their hypothesis using numerical simulations of VAM in delaminated composite plates. They studied damage indices based on various characteristics of spectrum of the dynamic response (magnitude of sidebands, probe frequency, pump frequency) of the plate and established the feasibility of VAM-based damage localization. Thus, the utility of the damage mapping scheme has been studied for homogeneous, anisotropic, thin composite plates by performing numerical experiments. However, researchers have not yet investigated the applicability of VAM-based damage mapping to detect and localize cracks in structural concrete components. We remark that thick, heterogeneous structural concrete components present significant challenges for VAM test set-up, data analytics, and damage mapping. In this report we discuss our experimental investigation into various aspects of ASR induced damage (crack) localization for concrete components using VAM testing.

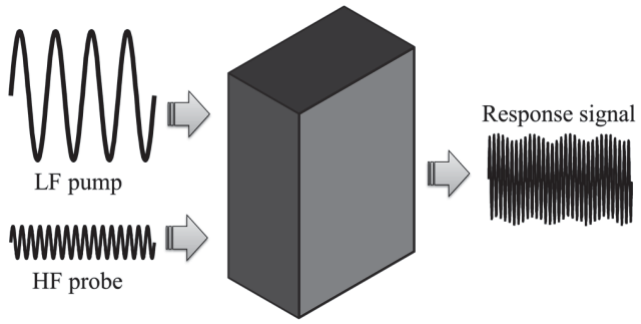

Figure 2: The principal of the VAM technique (Kim et al. 2014)

2.2.2 Digital Image Correlation

DIC is an optical non-contact NDE technique that is capable of measuring the deformation, displacement, and strain of a structure (Bruck et al. 2012). During the NPP routine pressure tests on containment vessels, when the internal pressure reaches 60 psi, it might be possible to use DIC to determine deformation of the concrete containment. DIC is capable of detecting surface defects, such as cracks, micro-cracks, and spalling, but it is unable to detect any subsurface defects.

The primary benefit of DIC is in measuring deformation. Therefore, of interest in this study is the ability of DIC to detect changes in the dimensions of the slab due to ASR gel expansion. DIC requires a speckled pattern on the specimen to anchor observations at different points in time. This also presents a problem for the cement brick specimens that are immersed in NaOH solution or water -- the pattern is disturbed and partly dissolved in the NaOH solution. However, if the cement brick specimen is cured above water, DIC might be applicable.

3. CONCRETE SAMPLES

In this work, we investigate the utility of the VAM and DIC techniques discussed in Section 2.2 for monitoring degradation in concrete samples due to ASR. The monitoring techniques are studied with concrete samples constructed and cured in the laboratory. These include: (1)a medium-sized concrete slab (without reinforcement) with pockets of reactive aggregate cast and cured at Vanderbilt University, Nashville, Tennessee; (2) a large reinforced concrete slab with reactive aggregates cast and cured at the UT, Knoxville, Tennessee and; (3) concrete blocks (without reinforcement) with reactive and non-reactive aggregates cast and cured at the University of Alabama, Tuscaloosa, Alabama. In particular, an uncertainty quantification methodology is developed with the VAM technique to quantify the uncertainty in diagnosis.

3.1 Medium-Sized Concrete Slab at Vanderbilt University

In this section, we discuss a medium-sized concrete slab of dimensions of 2 ft × 2 ft × 6 in. cast on December 21, 2015 and cured at Vanderbilt University. The details on casting and curing process of this concrete sample is discussed in detail the report by Mahadevan et al. (2016). Figure 3 shows an image of the slab immediately after the mold was removed.

Figure 3: 2 ft × 2 ft × 6 in. dimension concrete slab.

Four types of aggregate were placed in pockets at a depth of 3 in. in the four quadrants of the slab (Figure 4). The aggregates were placed in pockets instead of being dispersed throughout the slab so that the reactivity of each aggregate can be determined independently. Additionally, since the locations of the pockets of aggregate are known, this information was used to validate the localization of ASR from monitoring perspective. The four types of aggregates used are as follows:

1. Pure silica – powder from local ceramic shop
2. Maine – coarse aggregate from Maine, donated by University of Alabama
3. New Mexico – coarse aggregate from New Mexico, donated by University of Alabama
4. Ontario – coarse aggregate from a quarry in Ontario, Canada, donated by the Ontario Ministry of Transportation

From December 21, 2015 to September 2016, the medium-sized concrete slab did not show visual signs of degradation due to ASR. In October 2016, researchers observed the first visual evidence of degradation due to ASR. Since then, the degradation related damage has become increasingly pronounced. The first indication of damage was detected by the two vibration-based technique, NIRAS and VAM. Then researchers observed hairline cracks on the surface of the slab, and later, an ASR gel effluent and whitish

powder seeped out of the slab. In Figure 4, the red squares identify the locations where researchers observed seepage of ASR gel effluent on the sides of the slab. The seepage corresponding to locations marked in red squares in Figure 4 is shown in Figure 5, Figure 6, and Figure 7 respectively.

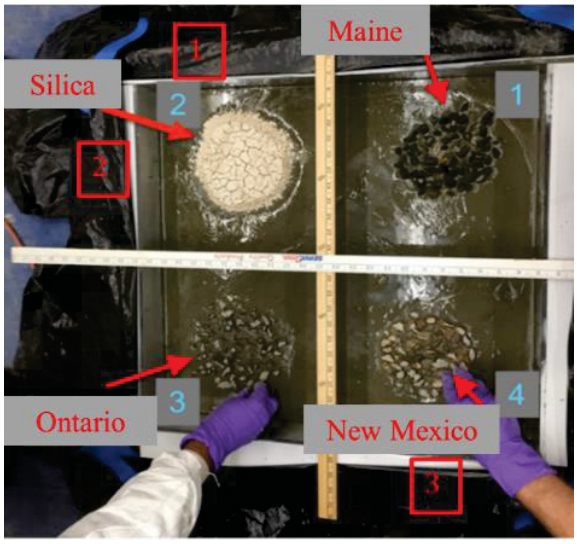

Figure 4: Pockets of aggregate in the slab during casting with red squares identifying visually observed cracks and effluence on the side of the slab.

Figure 5: Damage location 1 – cracking and powder effluence.

Figure 6: Damage location 2 – clear gel effluence.

Figure 7: Damage location 3 – cracking and powder effluence

4. LABORATORY TESTS FOR DAMAGE DETECTION AND LOCALIZATION USING VIBRO-ACOUSTIC MODULATION

VAM is a vibration-based method that utilizes signatures of nonlinear dynamic interactions on contact surfaces of cracks or delamination damage to detect and localize the damage. To the best of our knowledge, the applicability of VAM tests in detecting and localizing ASR induced damage (cracks) has not been studied in the laboratory. As a part of this research project, VAM tests are conducted on the medium-sized slab with reactive aggregate pockets at known locations, as well as on four concrete blocks cast using either reactive or non-reactive aggregates. We discuss our findings in this section.

4.1 VAM Test Setup for Experimental Analysis

Researchers can induce nonlinear dynamic interactions or a delamination at the surfaces of a crack using either an impact or VAM technique.

In the impact modulation mode, the impact-induced vibrations of the structure modulate a higher frequency at the damage interface to produce a dynamic signature of the nonlinearity. In our previous work, we tested this approach, but these experiments failed to produce clear indicators of nonlinearity in a specimen with ASR damage. Therefore, we use the VAM technique for all the experiments reported. In the VAM technique, the structural component of interest is excited using a lower "pump" frequency and a higher "probe" frequency. Nonlinear behavior at the interface (variable contact area or nonlinear adhesive bond at the interface) causes modulation of the probe frequency by the pump frequency. This can be seen as sidebands around the probe frequency in the spectra of measured response in a VAM test. In our laboratory experiments, we deliver the pump and probe excitations using piezo-stack actuators. We vary the locations of these actuators, as well as the frequencies at which they operate (i.e., the pump and probe frequencies).

We measure the response of the structural component of interest using a finite number of accelerometers placed on the surface of the component. The relative magnitudes of sidebands at various accelerometer locations are used to map the damage (ASR-induced cracks) in the component. The performance of the VAM test depends on the values of parameters used, as well as on the methodology used for processing the data collected during a VAM test. We discuss, next, various factors involved in the selection of test parameters (f_{pu}, f_{pr}) and data processing methods (baseline adjustment, sideband detection).

4.1.1 Pumping Frequency

In our laboratory experiments, we used the first fundamental frequency of the slab as well as an arbitrary low frequency as the f_{pu}. We estimated the fundamental frequency of the structural component by

conducting a hammer test. That is, we excited the structural component using an impact hammer and measured the acceleration at various locations using accelerometers. We computed the power spectral density (PSD) of the measured acceleration time series using the Welch's method (Welch, 1967).

The PSD shows multiple peaks that correspond to natural frequencies of the structure. The first and most prominent peak was assumed to be first modal frequency. For Vanderbilt's medium-sized slab, this value was 920 Hz. The frequency of 920 Hz was used as f_{pu} for his slab for all our experiments. For the Alabama samples 920 Hz was used as an arbitrary low f_{pu}, in addition to the first modal frequencies for each sample. Listed in Table 1 are the modal frequencies found using a hammer test for the Alabama samples.

Table 1: Experimental first modal frequency for each sample

Slab Sample	Approximate First Modal Frequency (Hz)
Vanderbilt's Medium Slab	920
Alabama- North Carolina Reactive	1865
Alabama- North Carolina Control (non-reactive)	2390
Alabama- Colorado Reactive	1695
Alabama- Colorado Control (non-reactive)	2240

4.1.2 Probing Frequency

It has been reported in the literature that the f_{pr} should be at least 10 to 20 times the pumping frequency (Singh et al. 2017). When the f_{pr} is N times the pumping frequency it allows for the crack to open and close N times in a pumping cycle. Thus, the ratio between the pump and probe decides the opportunity (number of times per cycle of pumping vibrations) for modulation to occur. In accordance with these guidelines, in our experiments we used probing frequencies ranging from 10 kHz to 21 kHz. The amplitude and location of the probing signal was also varied in different experiments.

In numerical studies the f_{pr} worked best for damage localization when it was $1/10^{th}$ the amplitude of the f_{pu}. In general, this is true for our experiments. The acceleration spectra plots do not show this clearly, because the ordinates of the spectra are multiplied by the square of the circular frequency. However, in linear spectra of displacements, the strength of the probing signal is always less than the strength of the pumping signal. In our experiments the pump and probe signal amplitudes were controlled by signal (function) generators. We used four amplitudes for the output voltage of the probing signal generator – 500 mV, 250 mV, 100 mV, or 50 mV. We maintained the output voltage of the pumping signal generator at 500 mV. The pumping and probing signals were amplified by an amplifier and sent to the piezo-stack actuator. A constant amplification factor (+28 dB) was maintained for all tests.

4.1.3 Accelerometers

A maximum of 21 accelerometers were placed on the concrete specimen at a time and connected to the data acquisition system. We varied the locations of these accelerometers for each experiment. The accelerometers had a sensitivity of 100 mV/g. In previous testing, we only used 12 accelerometers with a sensitivity of 10 mV/g.

4.2 Calculation of the Damage Index (Sideband Sums)

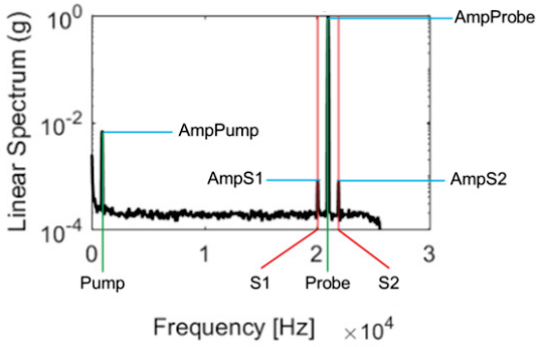

Figure 8: LS Plot for an accelerometer labeled to show the values used in calculating SBSum. SBSum=AmpS1+AmpS2.

In our laboratory experiments, multiple accelerometers were placed on concrete specimens cured in an aggressive environment (60ºC and 100% relative humidity) to encourage ASR. The slab was excited using a pump and a probe frequency, and we recorded the time history of accelerations at different locations on the surface of the slab. The LS of the noisy acceleration time history was computed using the Welch's method (Welch, 1967) with zero overlap and a Nuttall-defined, 2048-point, four-term, symmetric, Blackman-Harris window (Nuttal, 1981). Linear spectrum (LS) of the acceleration time history was computed from the PSD (Figure 8). The nonlinearity in the structural response, or the modulation of the f_{pr} by the f_{pu}, is seen as sidebands around the f_{pr} ("peaks" in the LS at frequencies equal to $(f_{pr} \pm f_{pu})$. After computing the LS, the values of AmpS1 and AmpS2 (Figure 8) were used to calculate the sideband sums (denoted as SBSum). In this report, we discuss mapping of ASR-induced cracks based on the SBSum metric, $\text{SBSum} = \text{AmpS1} + \text{AmpS2}$ (Figure 8).

4.3 Data Processing

The methodology for mapping damage using a sidebands-based damage index has been demonstrated using numerical simulations (Singh et al. 2017). However, the various practical aspects of the methodology haven't been studied. For example, the data collected in our experiments contains noise. For the experimentally collected data, the linear spectra in neighborhood of the sidebands do not show near-zero amplitudes at all sensor locations. Thus, an automated sideband detection algorithm may identify the *ambient* linear spectrum values at $(f_{pr} \pm f_{pu})$ as sidebands.

In processing the data, we conduct baseline adjustment and other sideband detection techniques. In baseline adjustment, we subtracted the average of the LS ordinates in the neighborhood of the sidebands from the sideband values calculated from the LS. An automated SBSum calculation process may also be misled by considering ordinates at given frequencies that are not peaks (and hence they do not indicate of nonlinear structural behavior). To ensure that the values being used to calculate SBSum are physically meaningful sidebands, we implemented a method for finding local peaks in the data. In this method, it was first determined whether the sideband value for a given frequency was a local peak. Next, we checked whether the sideband was a maximum value within a 1000 Hz window centered at the sideband frequency of interest. The ordinate value at a given frequency was selected as a sideband only if it satisfies both the conditions given above (Mahadevan et al. 2018).

4.4 VAM Results for the VU Slab

In this section, we report the results of VAM tests performed on the VU slab. In order to test the damage mapping capabilities of VAM-based diagnosis methodology, we divide the slab in four quadrants, and perform VAM test with a grid of 21 accelerometers for each half. The pump and the probe actuators are

placed at the center of each quadrant and the center of the slab (Figure 9). The blue and green circles represent the pump and probe actuators. We used different probing amplitudes (50 mV, 100 mV, 250 mV, and 500 mV) and probing frequencies of 10 kHz to 21 kHz (by 1000 Hz)) for VAM testing. The f_{pu} was 920 Hz with a 500 mV amplitude. We conduct VAM tests using these parameters for each quadrant, collect the acceleration time series data at each accelerometer location, compute the corresponding LS, and obtain SBSum metric. Next, we plot the variation of the SBSum metric over each quadrant using linear interpolation of the SBSum metric obtained at accelerometer locations. We juxtapose damage maps for the four quadrants in order to obtain a damage map for the entire slab. Figure 10 to Figure 12 show damage maps for three probing frequencies.

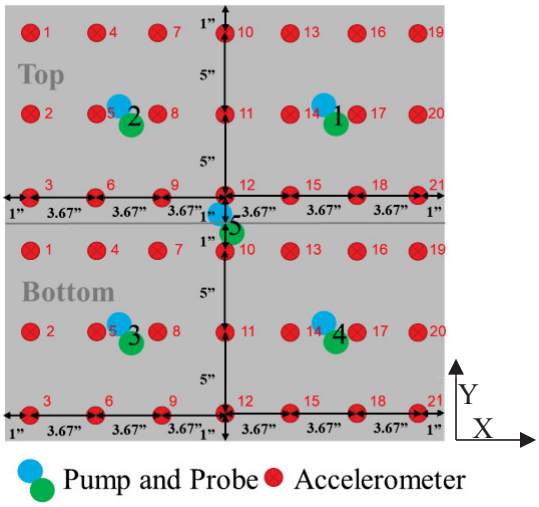

Figure 9: Pump, probe, and accelerometer locations for both halves of the slab (labeled in gray).

In Figure 10 to Figure 12, the locations of relatively higher SBSum values generally correspond to the locations of visible cracking and effluent seepage in the slab. There is a large crack located between quadrants 1 and 4. This crack is visible in Figure 11 and Figure 12. We also expect a large amount of damage near quadrants 2, 3 and 4, since there is an area of effluent seepage. This is seen in Figure 10 to Figure 12, where quadrants 3 and 4 consistently show higher SBsums.

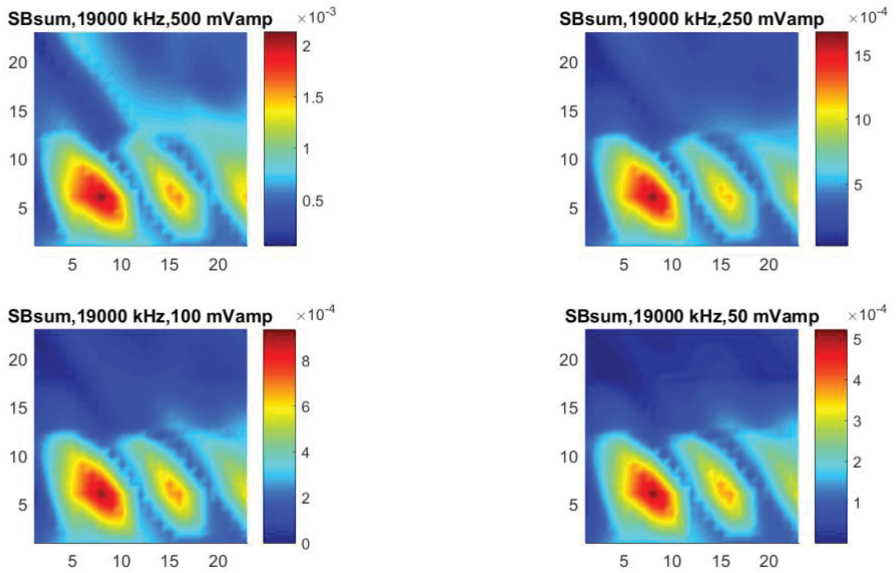

Figure 10: SBSum data in the linear spectrum of acceleration given a 500mV Pump of 920 kHz, and 500, 250, 100, and 50mV Probes of 19kHz for all 5 pump and probe locations.

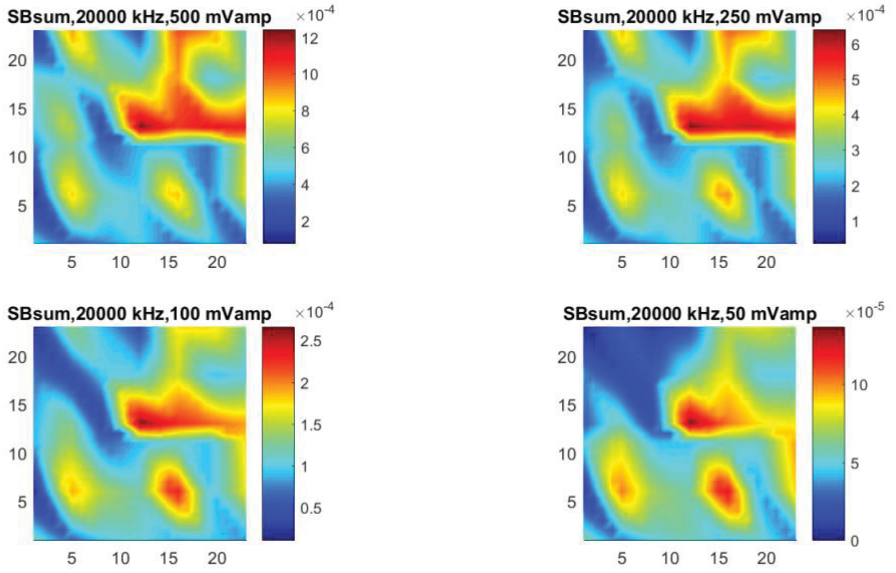

Figure 11: SBSum data in the linear spectrum of acceleration given a 500mV Pump of 920 kHz, and 500, 250, 100, and 50mV Probes of 20kHz for all 5 pump and probe locations.

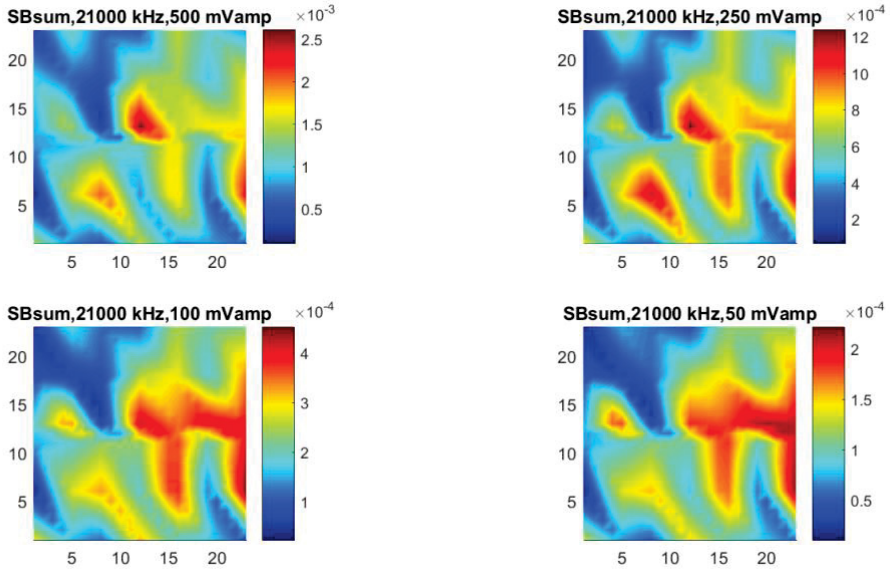

Figure 12: SBSum data in the linear spectrum of acceleration given a 500mV Pump of 920 kHz, and 500, 250, 100, and 50mV Probes of 21 kHz for all 5 pump and probe locations.

4.5 VAM Results for the Alabama Slabs

In this section are reports from VAM test results for four concrete slabs received from the University of Alabama. Two of the slabs were cast using reactive aggregate, and the remaining two slabs were cast using non-reactive aggregate. We perform VAM tests and we compare the magnitude of damage indices for slabs cast using reactive and non-reactive aggregate. We use a grid of 21 accelerometers for VAM testing of the Alabama slabs. Figure 13 shows locations of accelerometers as well as pumping and probing actuators. We perform the VAM test, acquire acceleration data for each pump/probe location, compute the damage index (SBSum) using the baseline adjustment method, and sum the damage indices calculated for 10 sets of pump/probe locations. We use linear interpolation to obtain damage index variation (damage map) over the top surface of the slab.

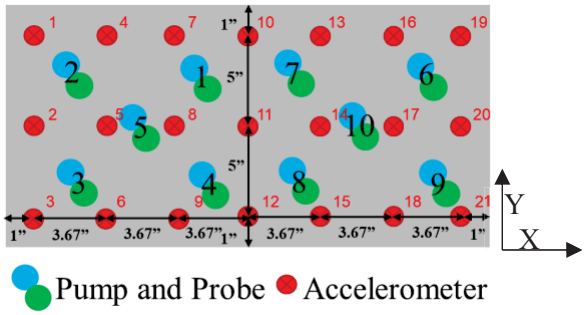

Figure 13: Accelerometer and pump and probe actuators placement for the Alabama samples.

The LS for acceleration shows high-magnitude sidebands for the reactive samples and no sidebands for the control (non-reactive) samples. This simple observation suggests that VAM tests can be used for detection of ASR damage in concrete. The reactive samples show surface cracking, whereas the control (non-reactive) samples for both North Carolina and Colorado aggregates do not.

We perform damage mapping for the Alabama samples using the described method of calculating SBsum values. Figure 14 to Figure 17 show damage maps for the pump magnitude of 500mV, the pump frequency of 1695 Hz (Table 1), the probe frequency of 19 kHz and four probe amplitude values (50mV, 100 mV, 250 mV and 500mV). The results for the Colorado Reactive (Figure 14) North Carolina Reactive (Figure 16) show a consistent pattern for the distribution of SBSum values. The North Carolina and Colorado Reactive samples also show consistently high sidebands for the same region for all probe amplitudes. The results for the reactive samples are more consistent for all probing amplitudes, whereas for the control samples (Figure 15 and Figure 17), there is no consistency in the values of damage index at a particular region on the slab. The control samples also show lower SBsum values for the surface. The larger values found along the sides could be an outcome of boundary effect.

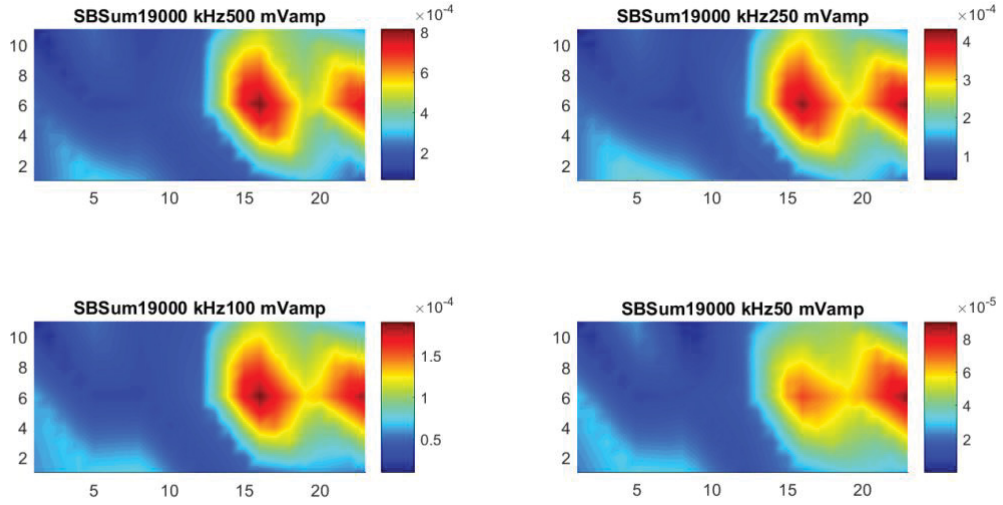

Figure 14: SBSum surface diagram for the Colorado Reactive sample with a 1695Hz and 500mV pump and a 21kHz probe of various amplitudes using a local peak filter.

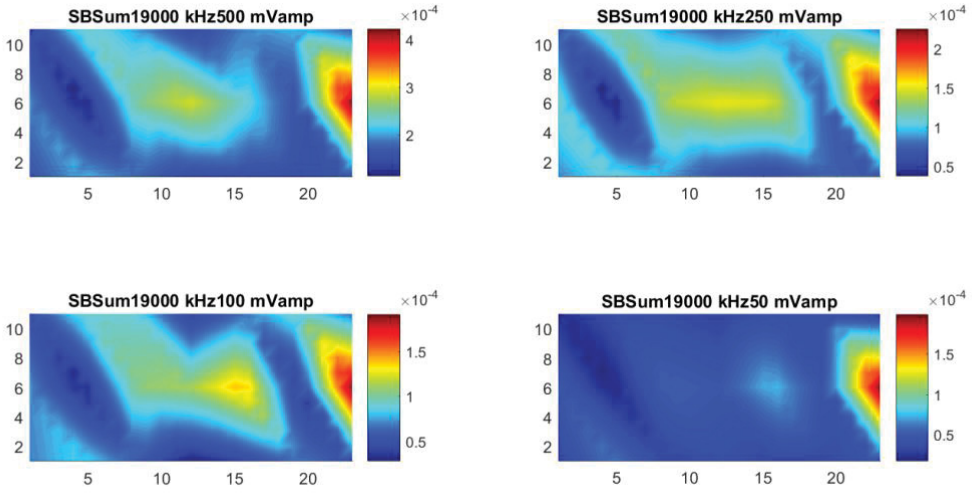

Figure 15: SBSum surface diagram for the Colorado Control (non-reactive) sample with a 2240Hz and 500mV pump and a 21kHz probe of various amplitudes using a local peak filter.

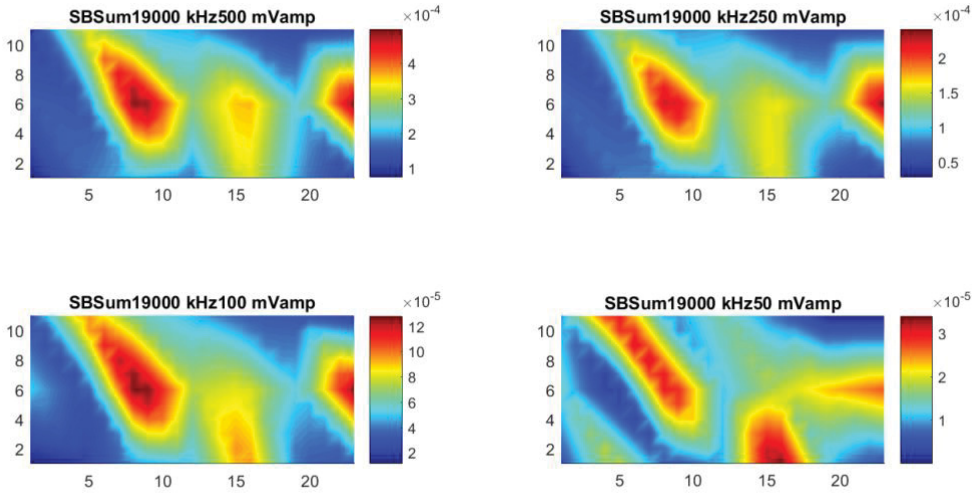

Figure 16: SBSum surface diagram for the North Carolina Reactive sample with a 1865Hz and 500mV pump and a 19 kHz probe of various amplitudes using a local peak filter.

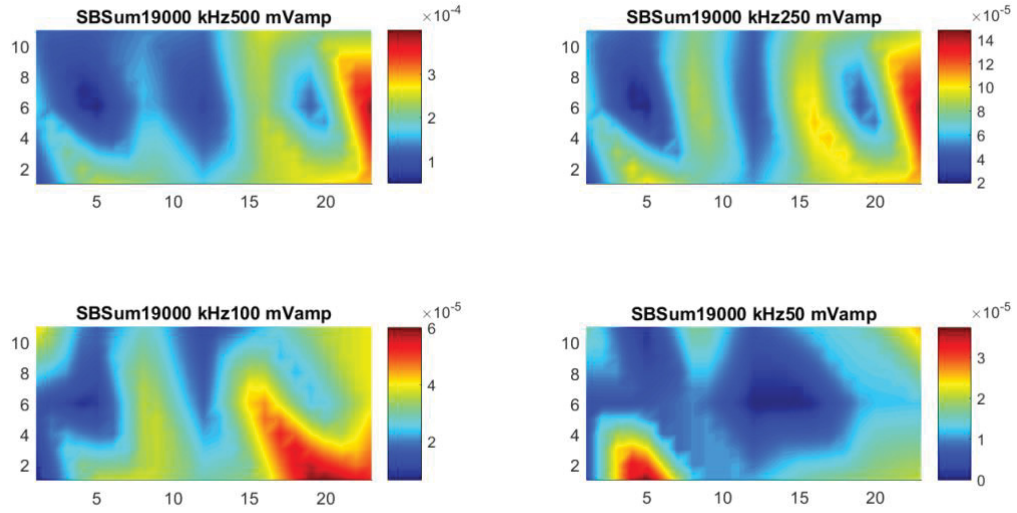

Figure 17: SBSum surface diagram for the North Carolina Control (non-reactive) sample with a 2390Hz and 500mV pump and a probe of various amplitudes using a local peak filter.

4.6 Summary of VAM Results

In this section, we discussed the results of laboratory experiments aimed at determining the effectiveness of VAM tests for detection and localization of ASR-induced cracks in structural concrete components. We performed VAM-based diagnosis of a medium-sized slab containing pockets of reactive aggregates at known locations, as well as two sets of two slabs cast using either reactive or non-reactive

aggregate (mixed throughout the slab). We used a damage index based on sidebands present in the linear spectrum of nonlinear dynamic structural response to map the distribution of damage in the concrete slab. We discussed some practical aspects of data processing and noise reduction involved in VAM testing for real structures. We found that the fundamental frequency of the structure (obtained using a hammer test) is the best choice for the pump frequency. For the medium-sized slab containing pockets of reactive aggregate at known locations, VAM-based damage mapping revealed damage signatures at locations that showed visible signs of ASR damage. The damage map also matched the expected extent of damage based on the reactivity of aggregates, i.e., the damage index showed highest damage where pure silica was placed as aggregate. For both sets of two Alabama slabs cast using either reactive or non-reactive aggregates, the VAM test consistently showed higher sidebands for the slab containing reactive aggregate.

5. UNCERTAINTY QUANTIFICATION IN DIAGNOSIS

Uncertainty quantification consists of two types of problems – forward problem of uncertainty propagation, and inverse problem of statistical inference. In the context of structural health monitoring, the forward problem is useful in prognosis; it uses Monte Carlo sampling to propagate uncertainty quantities through the model of the system to quantify the uncertainty in the model-based prediction of the system performance (e.g., damage growth). The inverse problem is useful in diagnosis, where the observed data is used to infer the state of damage in the structure. The Bayesian approach used in this study for the inverse problem requires Markov Chain Monte Carlo sampling. Both the basic and Markov chain-based sampling techniques require a large number of evaluations of the physics model, which can be prohibitively expensive. Therefore an inexpensive surrogate model is first trained using physics model runs, and the surrogate model can be used for diagnosis and prognosis uncertainty quantification.

In other cases, a physics model may not be available. In that case, a data-driven surrogate model connecting the inputs and the output is constructed based on experimental observations, making surrogate model construction is an important first step in uncertainty quantification. The surrogate model in this study is built using the VAM experimental data collected on the Vanderbilt and Alabama slabs; the data collection and analyses were described in the previous sections, and the surrogate model construction is described in this section.

5.1 Neural Network

Many types of surrogate modeling techniques have been studied in the literature, such as simple regression fits, polynomial chaos, radial basis functions, Kriging, support vector machines, and neural networks. The neural network approach is pursued in this study to train a data-driven model to predict SBSUM, as a function of various testing parameters (such as probe frequency, and amplitudes of pump and probe excitations). The neural network approach has the advantage of being able to process large amounts of data that are likely to be available in the monitoring actual NPP structures.

An artificial neural network consists of functions arranged in a series of layers. Input values feed into the system and pass through the hidden layers before arriving at the output value for that input. The learning method is backpropagation, where the difference between the output of the network and the actual output is minimized (Lapedes, 1988). The neural network used for the Vanderbilt slab is shown in Figure 18. It considers 6 inputs: Probing excitation frequency, probing excitation amplitude, X coordinate of the pump and probe location, Y coordinate of the pump and probe location, X coordinate of the accelerometer location, and Y coordinate of the accelerometer location. The output variable is SBsum. The model has 40 hidden layers and uses the Levenberg-Marquardt method for training.

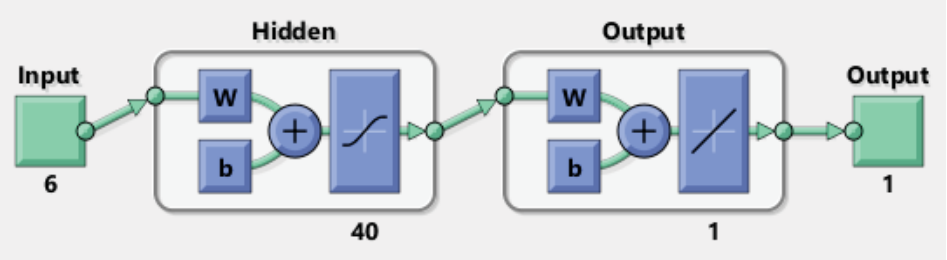

Figure 18: Neural Network for the Vanderbilt slab with 6 inputs, 1 output, and using 40 layers.

The data was split for training (70%), testing (15%), and validation (15%) of the model. Figure 19 shows the regression plots for the data. Overall the fit of the model is moderate; however, the error histogram in Figure 20 shows error close to zero; also, the model had a very low mean square error value.

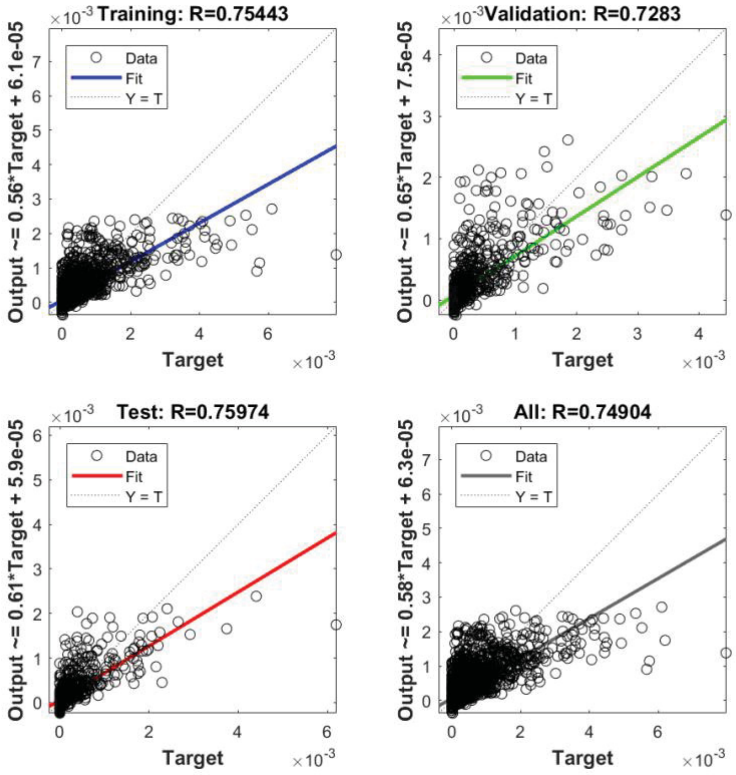

Figure 19: Regression plots for the Vanderbilt slab neural network.

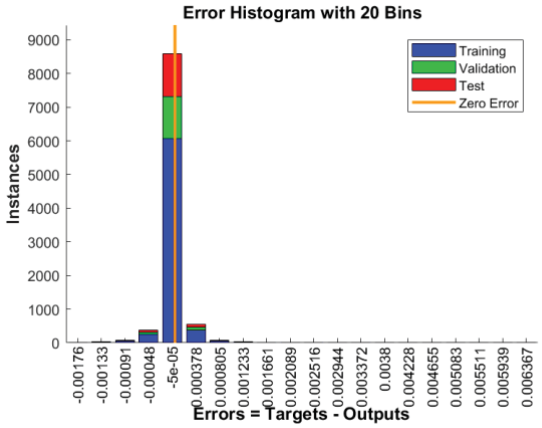

Figure 20: Histogram of errors using the Vanderbilt slab neural network model.

In order to demonstrate the performance of the predictive model, we compare the output of the model with experimental results. Figure 21 and Figure 23 show the experimental results from the SBsum and Figure 22 and Figure 24 are the results corresponding same test parameter values from the prediction model. For Figure 22 the probing frequency is 20 kHz and the amplitude is 500 mV with the pump and probe at the center of the slab. The overall area of damage in the predicted model is similar to the experimental results in Figure 21. For Figure 24 the probing frequency of 16 kHz and the amplitude is 100 mV with the pump and probe at the center of quadrant 2. Again, the predicted damage area was similar to the experimental results in Figure 23. The higher SBsum values are at the top-center of the slab for both. The value of the predicted SBsum is also in the same magnitude as the actual results for both examples.

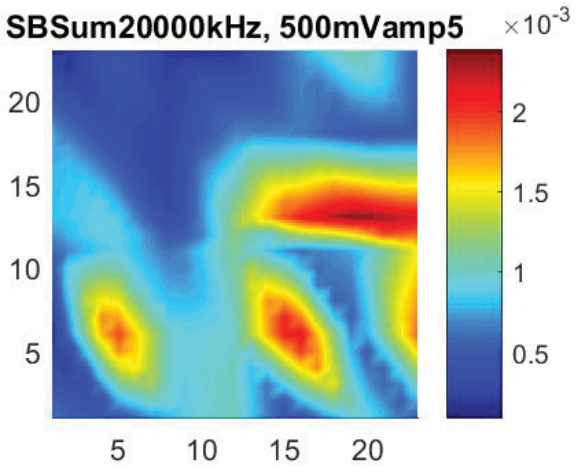

Figure 21: Experimental SBsum results of the Vanderbilt slab using a probing frequency of 20 kHz, a probing amplitude of 500 mV and the pump and probe in the center of the slab.

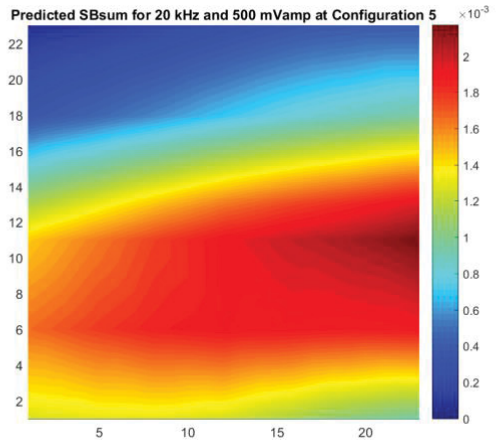

Figure 22: Neural Network SBsum results of the Vanderbilt slab using a probing frequency of 20 kHz, a probing amplitude of 500 mV and the pump and probe in the center of the slab.

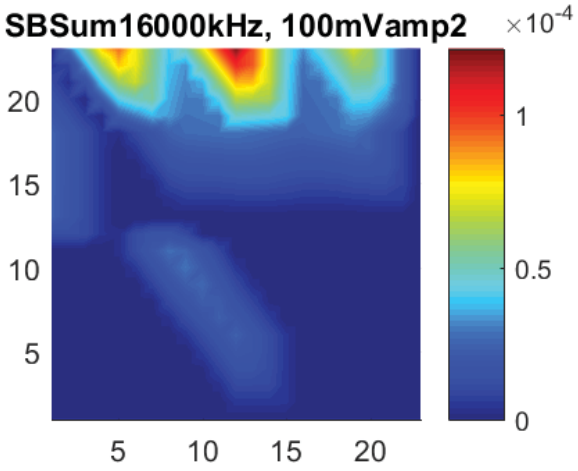

Figure 23: Experimental SBsum results of the Vanderbilt slab using a probing frequency of 20 kHz, a probing amplitude of 100 mV and the pump and probe in the center of quadrant 2.

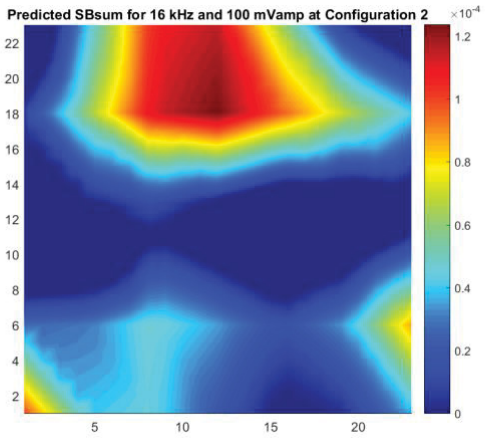

Figure 24: Neural network SBsum results of the Vanderbilt slab using a probing frequency of 16 kHz, a probing amplitude of 100 mV and the pump and probe in the center of quadrant 2.

A neural network was also trained to predict the SBsum values for the North Carolina Reactive sample. This model used the same 6 inputs and outputs as the Vanderbilt model, but has 75 layers, instead of 40. The regression for the training, testing, and validation data is shown in Figure 25. Similar to the Vanderbilt model, the regression is not very good, but the overall error in the model remains low (Figure 26).

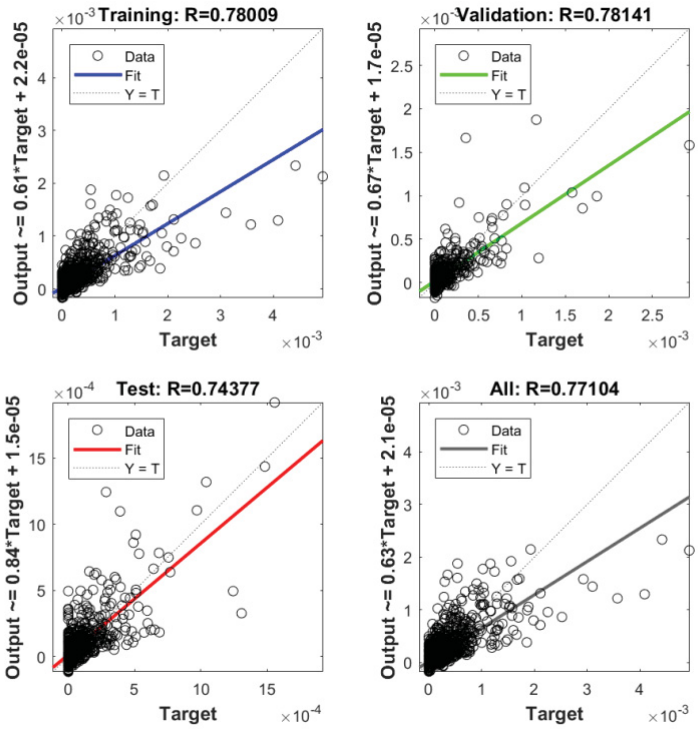

Figure 25: Plots of the regression for the North Carolina Reactive sample neural network.

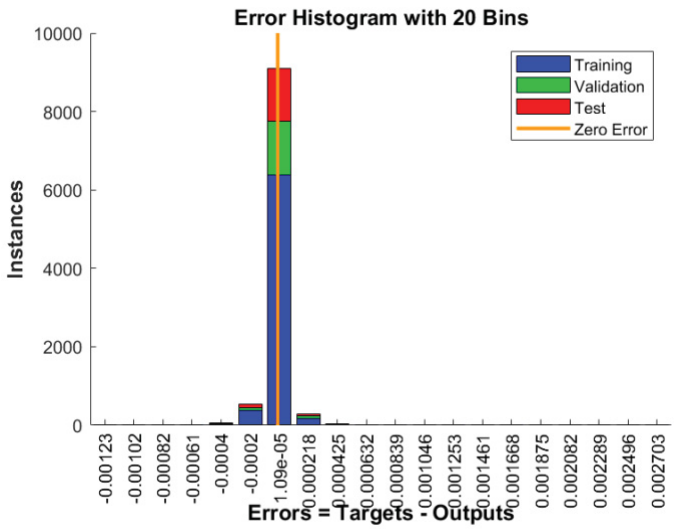

Figure 26: Error histogram for the North Carolina Reactive sample neural network.

Again, we compare the output of the data-based model with experimental results. Figure 27 and Figure 29 show the experimental results, and Figure 28 and Figure 30 are the corresponding results from the prediction model. For Figure 28 the probing frequency is 21 kHz and the amplitude is 500 mV with the pump and probe at configuration 10 (Figure 13). The overall area of damage predicted by the model is similar to the experimental results in Figure 27. Sensors with higher SBsum values are located on the right side of the slab for both images. For Figure 30 the probing frequency of 18 kHz and the amplitude is 250 mV with the pump and probe are at configuration 7 (Figure 13). Again, the predicted damage area was similar to the actual results in Figure 29. The value of the predicted SBsum is also in the same magnitude as the actual results for both examples.

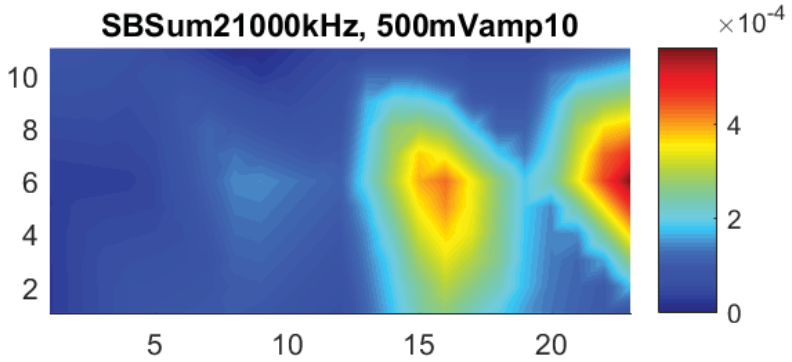

Figure 27: Experimental SBsum results of the North Carolina Reactive sample using a probing frequency of 21 kHz, a probing amplitude of 500 mV and the pump and probe at configuration 10 (Figure 13).

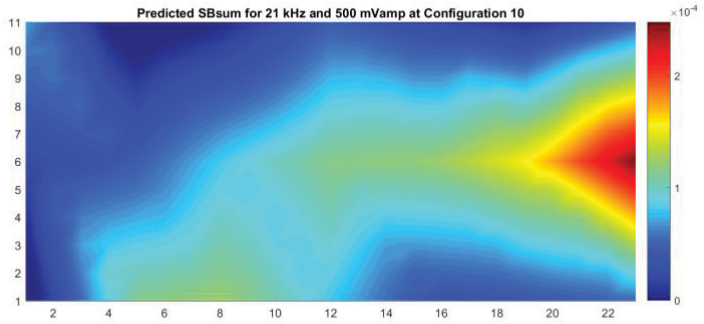

Figure 28: Neural network SBsum results of the North Carolina Reactive sample using a probing frequency of 21 kHz, a probing amplitude of 500 mV and the pump and probe at configuration 10 (Figure 13).

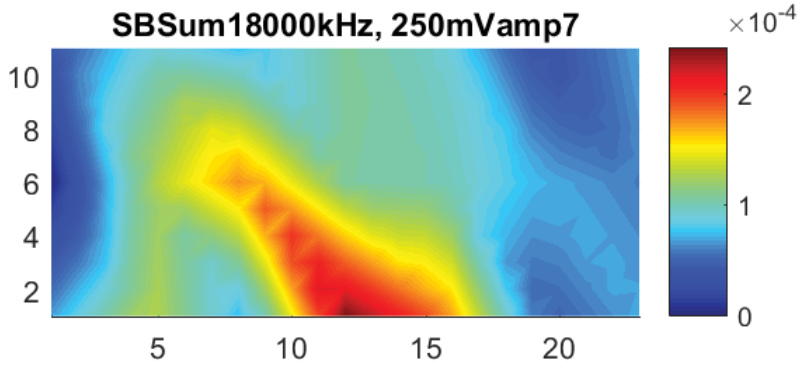

Figure 29: Experimental SBsum results of the North Carolina Reactive sample using a probing frequency of 18 kHz, a probing amplitude of 250 mV and the pump and probe at configuration 7 (Figure 13).

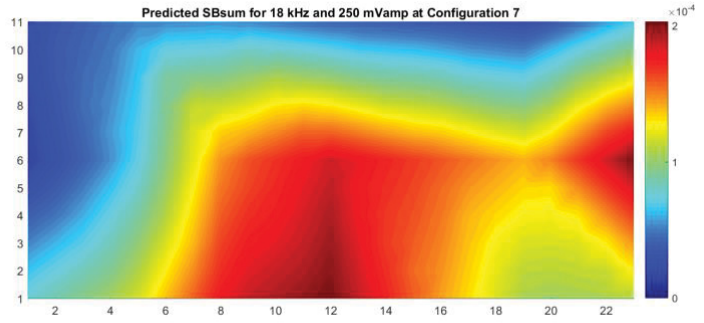

Figure 30: Neural network SBsum results of the North Carolina Reactive sample using probing frequency of 18 kHz, a probing amplitude of 250 mV and the pump and probe at configuration 7 (Figure 13).

The neural network used to train the model for the Colorado Reactive sample used the same 6 inputs and outputs as the Vanderbilt and North Carolina models. The network used 80 layers. Figure 31 shows

the regression for the training, testing, and validation data. Figure 32 shows the error histogram. This model had the highest regression.

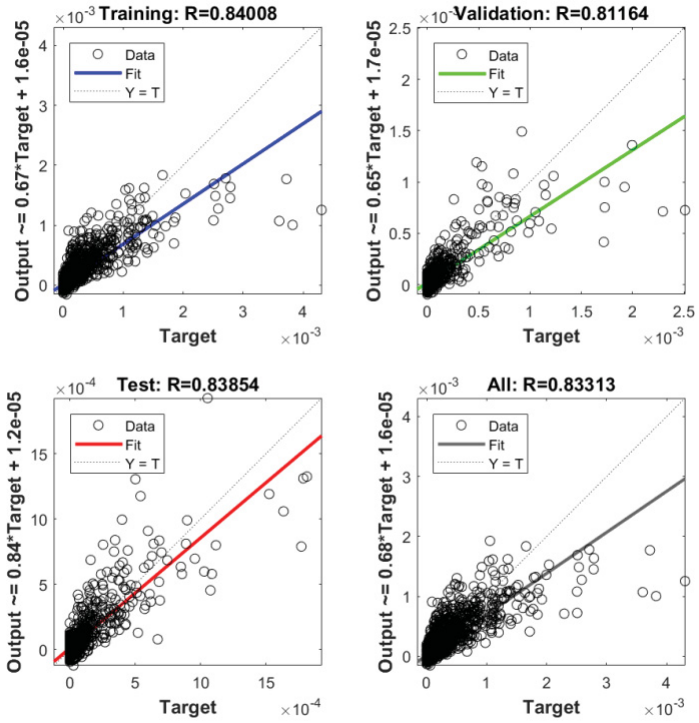

Figure 31: Plots of the regression for the Colorado Reactive sample neural network.

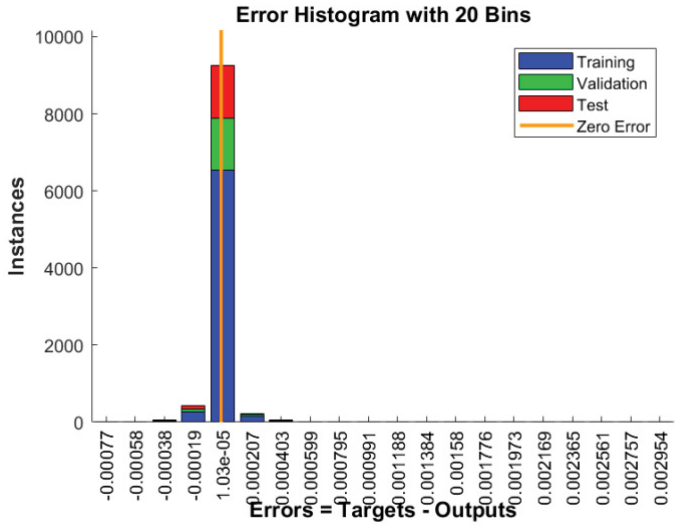

Figure 32: Error histogram for the Colorado Reactive sample neural network.

Figure 33 and Figure 35 show the actual experimental results from the SBsum and Figure 34 and Figure 36 are the corresponding results from the prediction model. For Figure 34 the probing frequency is 21 kHz and the amplitude is 500 mV with the pump and probe at configuration 10 (Figure 13). The overall area of damage in the predicted model is similar to the experimental results in Figure 33. The higher SBsum is located at the right side of the slab for both images. For Figure 36 the probing frequency

is 18 kHz and the amplitude of 250 mV with the pump and probe at configuration 7 (Figure 13). Again, the predicted damage area was similar to the actual results in Figure 35.

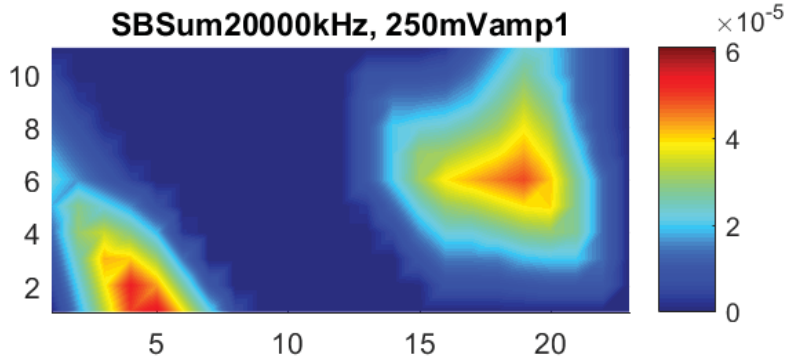

Figure 33: Experimental SBsum results of the Colorado Reactive sample using a probing frequency of 20 kHz, a probing amplitude of 250 mV and the pump and probe at configuration 1 (Figure 13).

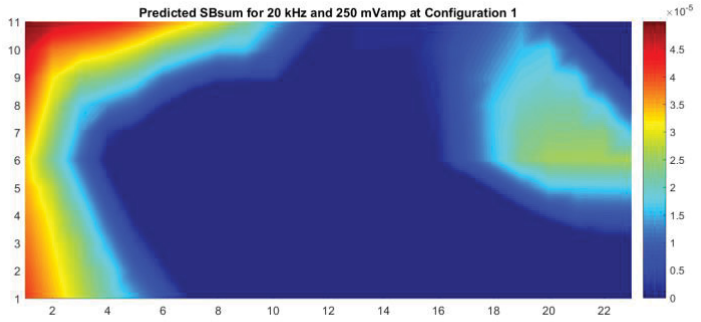

Figure 34: Neural network SBsum results of the Colorado Reactive sample using a probing frequency of 20 kHz, a probing amplitude of 250 mV and the pump and probe at configuration 1 (Figure 13).

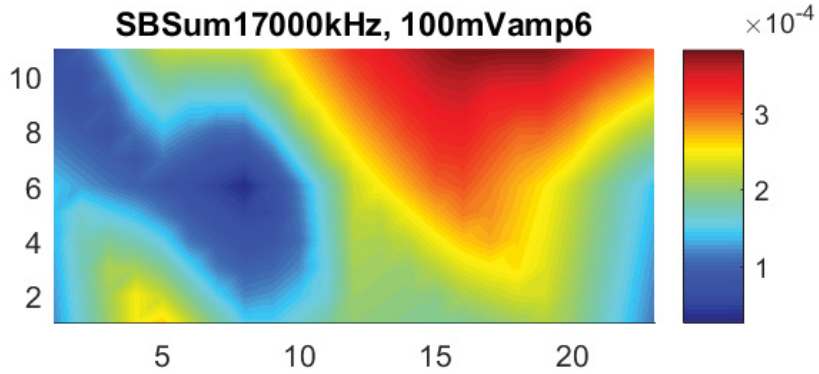

Figure 35: Experimental SBsum results of the Colorado Reactive sample using a probing frequency of 17 kHz, a probing amplitude of 100 mV and the pump and probe at configuration 6 (Figure 13).

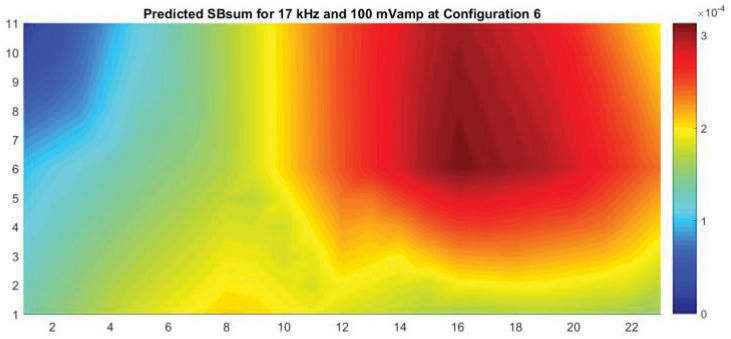

Figure 36: Neural network SBsum results of the Colorado Reactive sample using a probing frequency of 17 kHz, a probing amplitude of 100 mV and the pump and probe at configuration 6 (Figure 13).

5.2 Sensitivity Analysis

One of the benefits of the surrogate model built in Section 5.1 is the ability to perform sensitivity analysis, to assess the relative contributions of the various experimental parameters to the overall uncertainty in the model prediction. Sensitivity analysis can be local or global; local sensitivity analysis is based on derivatives, whereas global sensitivity analysis estimates the contribution of the entire range of variation of the experimental parameter to the variance of the model output. Global sensitivity analysis is much more appropriate and useful in the context of this study.

Global sensitivity analysis estimates the contribution of each input variable to the variance of the model output. In the context of this study, "model" refers to the neural network surrogate model. "Inputs" refers to the experimental parameters (pump and probe frequencies, amplitudes, and locations). The "output" refers to SBSUM, the sum of the sideband amplitudes. The contribution to output variance is estimated using Sobol sensitivity indices, measuring either individual effect of each input separately, or the interactive effect of multiple inputs.

Consider a computational model in the form of $y = f(\boldsymbol{x})$ where $\boldsymbol{x} = \{x_1, \dots, x_k\}$ is the vector of stochastic model inputs. The first-order (individual effect) Sobol' index $S_i (i = 1,2, \dots, k)$ is

$$S_i = \frac{V_{x_i}\left(E_{\boldsymbol{x}_{-i}}(y|x_i)\right)}{V(y)} = 1 - \frac{E_{x_i}\left(V_{\boldsymbol{x}_{-i}}(y|x_i)\right)}{V(y)} \tag{1}$$

where $\boldsymbol{x}_{-i}$ means all the model inputs other than x_i. S_i quantifies the contribution of input x_i by itself to the uncertainty in output y. The total effects index S_i^T for X_i is the total contribution of X_i by itself as well as due to interactions with other inputs. The S_i^T can be computed as:

$$S_i^T = 1 - \frac{V\left(E(Y|X_{-i})\right)}{V(Y)} \tag{2}$$

The individual effects and total effects indices of the inputs can be computed using Monte Carlo sampling using the neural network surrogate model. In order to do this, the probability distributions of the inputs need to be characterized. In this study, all the inputs (experimental parameters) are controlled by the experimentalist and a range of values are chosen; therefore, it is appropriate to use uniform distributions to represent the variability of the experimental parameters. These statistics are shown in Table 2. The results of sensitivity analysis, based on 10000 Monte Carlo samples, are shown in Tables 3 to 5.

The sensitivity of each variable using the Vanderbilt slab neural network (Figure 18) shown in Table 3 indicates that the significant variables for the Vanderbilt prediction model are probing frequency, and the configuration location. The sensitivity for the North Carolina Reactive variables (Table 4) and the Colorado Reactive variables (Table 5), are similar to the Vanderbilt sample sensitivities: the predicted SBsum value is highly dependent upon the configuration location of the pump and probing actuators. The major difference between the models is that the first-order indices of the probing frequency in the North Carolina and Colorado Reactive sample models are not high, therefore the variable is not very significant in these models. Note that the Vanderbilt slab has four specific pockets of aggregates midway through the thickness of the slab, whereas the Alabama slabs have aggregates distributed throughout the samples. This difference in configuration explains the difference in sensitivity results for the two slabs.

Table 2: Variable range for uniform sampling

Variable	Range
Probing Frequency	10000-21000
Probing Amplitude	50-500
Pump and Probe Location X	0-24
Pump and Probe Location Y	0-12 or 0-24
Accelerometer X	0-24
Accelerometer Y	0-12 or 0-24

Table 3: Sensitivity analysis of the neural network for the Vanderbilt sample.

Variable	First-order Index	Total Effects
Probing Frequency	0.2553	1.0228
Probing Amplitude	0.0608	0.3365
Pump and Probe Location X	0.1731	2.5286
Pump and Probe Location Y	0.4771	2.9082
Accelerometer X	0.0182	0.1083
Accelerometer Y	0.0156	1.6438

Table 4: Sensitivity analysis of the neural network for the North Carolina Reactive sample.

Variable	First-order Index	Total Effects
Probing Frequency	0.0053	0.8096
Probing Amplitude	0.0381	0.3696
Pump and Probe Location X	0.0022	1.7035
Pump and Probe Location Y	0.9172	3.2141
Accelerometer X	0.0115	0.2062
Accelerometer Y	0.0257	0.2903

Table 5: Sensitivity analysis of the neural network for the Colorado Reactive sample.

Variable	First-order Index	Total Effects
Probing Frequency	0.0553	0.2540
Probing Amplitude	0.0472	0.4937
Pump and Probe Location X	0.3493	0.9646
Pump and Probe Location Y	0.5240	1.2955
Accelerometer X	0.0186	0.1411
Accelerometer Y	0.0056	0.1008

5.3 Damage Probability

Due to the presence of multiple sources of uncertainty, the presence of damage in any particular location cannot be determined as a "yes" or "no" result. Instead, this section develops a methodology to obtain an estimate of damage probability at each location in the slab, thus accounting for the uncertainty. This can be done using either the experimental data or the neural network surrogate models. Here, we study both approaches.

With respect to experimental data, researchers performed VAM tests using multiple combinations of test parameters (probe frequency, probe amplitude, pump/probe location). Damage probability can be approximately measured by determining how frequently damage is detected at a given sensor over all the test combinations. VAM-based damage detection method utilizes "relative" magnitude of SBsum at sensor locations to determine the presence of damage. Therefore, for each test, we compute the mean value and standard deviation of SBsum values computed at all sensor locations. The sensors exhibiting an SBsum value at least one standard deviation away from the mean SBsum value are marked as sensors showing the presence of damage. We count how often a given sensor showed the presence of damage in all our tests. We expect that the probability of damage will be higher in the vicinity of a sensor that consistently shows the presence of damage (i.e. a sensor at which the SBsum value is most frequently at least one standard deviation away from the mean).

Figure 37 to Figure 39 show the estimated damage probabilities using the above method for the experimental test data on the concrete slab specimens. The Vanderbilt sample shows the highest probability of damage in quadrants 3 and 4, and in between quadrants 1 and 4 (Figure 37). We can currently see a large crack in the slab between quadrants 1 and 4. The highest probability of damage in the North Carolina reactive aggregate sample occurs at accelerometers 8 and 20 (Figure 38). This area corresponds to the sensors that are most excited in Figure 16. For the Colorado reactive aggregate sample, the highest probability of damage occurs around sensors 14, 17, and 20; located in the center of the right side of the slab.

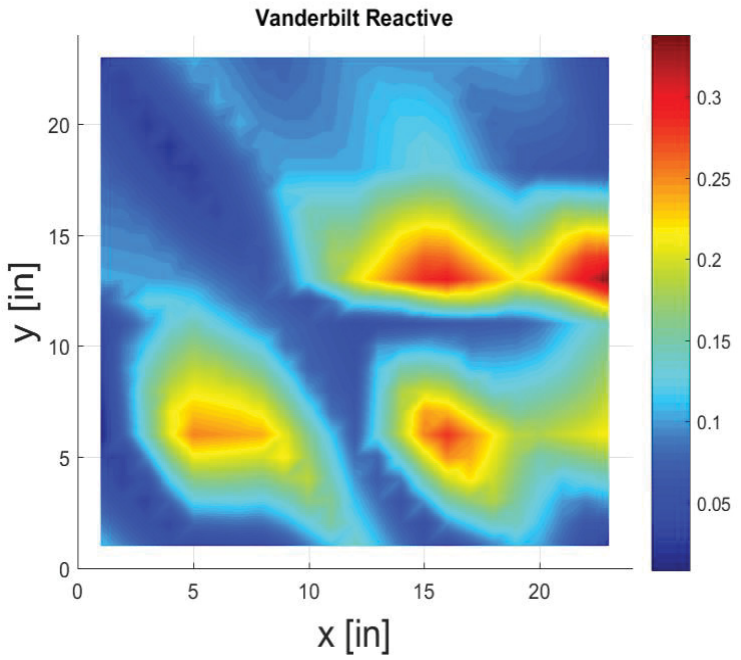

Figure 37: Damage probability map (using experimental data) for the Vanderbilt sample.

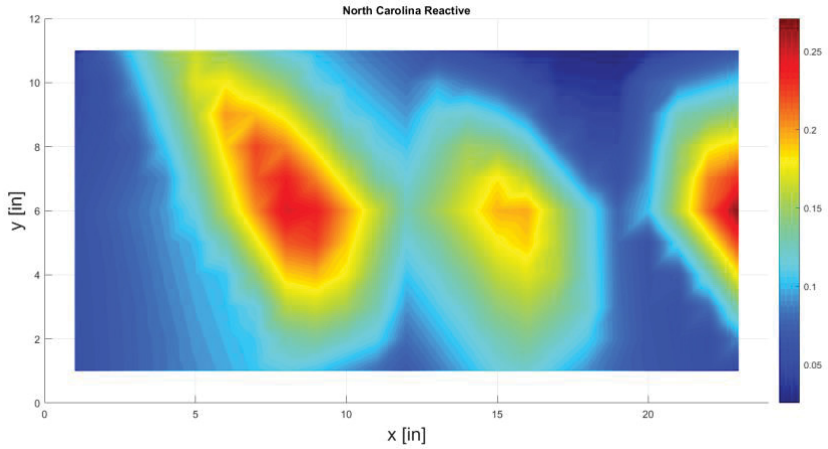

Figure 38: Damage probability map (using experimental data) for the North Carolina Reactive sample.

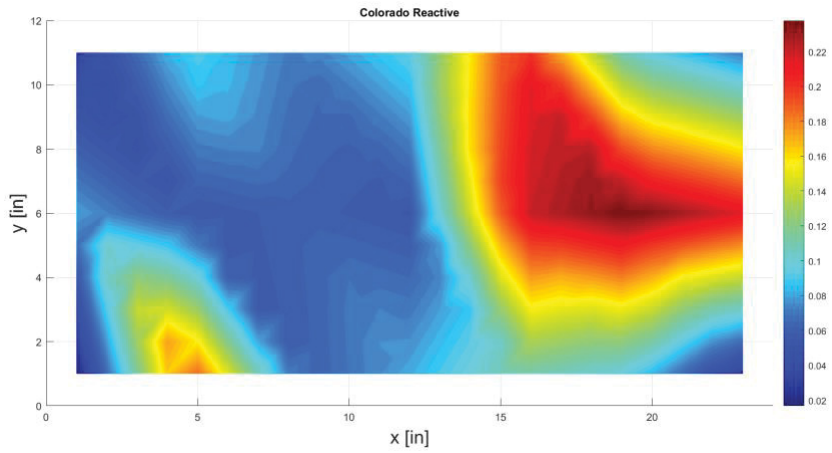

Figure 39: Damage probability map (using experimental data) for the Colorado Reactive sample.

The neural network surrogate model developed in Section 5.1 can also be used for uncertainty quantification in diagnosis and compute the damage probabilities at different locations in the slab. The same Monte Carlo samples that were generated for the sensitivity analysis in Section 5.2 can be used for this purpose. The samples of the inputs are drawn based on the distributions listed in Table 1, and propagated through the neural network surrogate model to calculate the corresponding value of SBSUM. Based on these results, the statistics of SBSUM at each location can be calculated, reflecting the uncertainty in SBSUM.

Each location is identified as damaged or not based on whether its SBSUM value exceeds a specified threshold value. Once the distribution of SBSUM at any location is obtained as above, it is straightforward to calculate the probability of damage at any location based on the same Monte Carlo samples generated above. Using this calculation, the uncertainty in the diagnosis result is quantified as the probability of damage at any location.

In order to compare the neural network prediction with the experimental data in terms of quantifying the uncertainty in damage diagnosis, here we simply duplicated the experimental conditions using the neural network model. Thus, the same conditions used in the experiments are used as inputs to the neural network model, and the output SBSUM values at the different sensor locations are noted. Then the damage probability maps are developed in the same manner as with experimental data above.

Figure 40 to Figure 42 show the estimated damage probabilities using the SBsum values predicted by the neural network model. The Vanderbilt sample shows the highest probability of damage in quadrants 1, 3 and 4, and in between quadrants 1 and 4 (Figure 40). The predicted model shows a lower probability of damage in quadrant 3 than the experimental results. The highest probability of damage in the North Carolina Reactive sample occurs at accelerometers 8 and 20 (Figure 41). These are the same locations as the experimental data shows (Figure 38). For the Colorado Reactive sample, the highest probability of damage occurs around sensors 1, 14, 16, 17, and 20; located in the center of the right side of the slab (Figure 42). These results for the predictive models of all of the samples are similar to the damage probabilities seen with the experimental results.

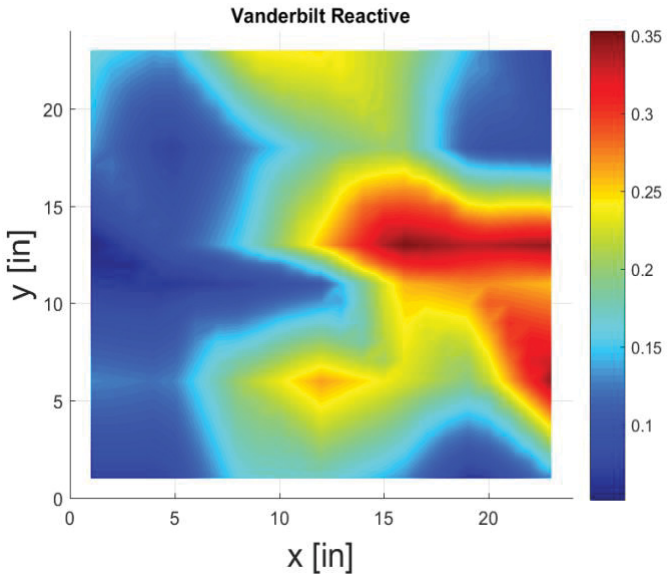

Figure 40: Damage probability map (using neural network) for the Vanderbilt sample.

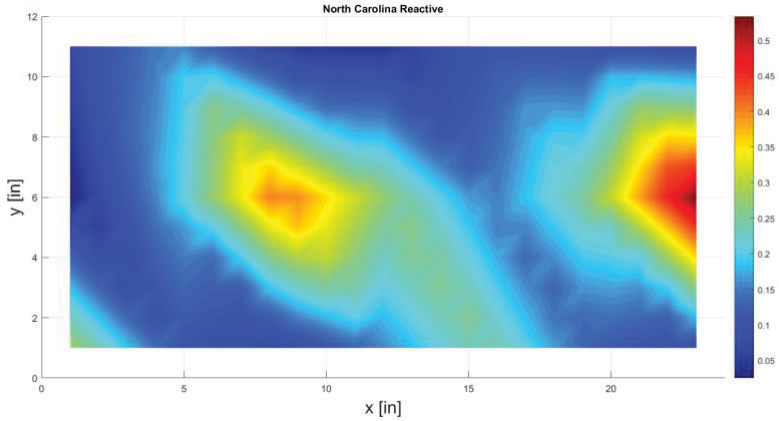

Figure 41: Damage probability map (using neural network) for the North Carolina Reactive sample.

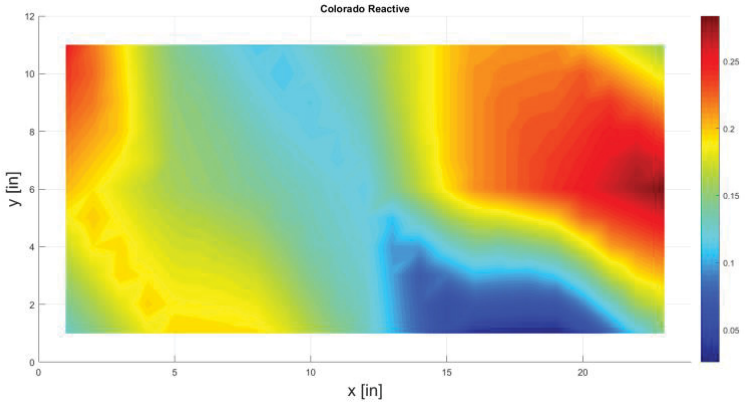

Figure 42: Damage probability map (using neural network) for the Colorado Reactive sample.

The damage probability maps integrate the results of multiple experimental conditions to quantify the uncertainty in diagnosis, and provide practical decision support for prognostics and health management (PHM). As noticed in Section 4, different experimental conditions gave different inferences regarding the presence of damage at any location. The proposed damage probability method integrates the inferences over all the experimental conditions. The agreement between the experimentally estimated damage probability maps and the surrogate model-predicted damage probability maps is encouraging. The benefit of the neural network is the ability to predict the SBSUM value at any location, and not being limited only to sensor locations as in the experiments. Limitations of resources, space, time, accessibility, etc. would limit the number of sensors that can be placed in experimental data collection. This means the neural network can be trained with the experimental data to predict the damage probability at any location on the specimen, for any combination of experimental parameters. The additional important benefit of the neural network model is sensitivity analysis, as detailed in the previous subsection.

6. LABORATORY TESTS FOR DAMAGE DETECTION USING DIGITAL IMAGE CORRELATION

The DIC technique was applied to the large concrete slab cast at the University of Tennessee, Knoxville. Digital DIC is a three-dimensional, full-field, optical NDE technique to measure contour, deformation, vibration, and strain. The technique can be used for many tests, including tensile, torsion, bending, and combined loading for both static and dynamics applications.

6.1 DIC Test Setup

An experimental setup for three-dimensional DIC and data analysis includes following steps:

1. Preparation: Two cameras are mounted at either end of a tripod camera (base) bar so researchers know the relative position and orientation of the two cameras with respect to each other. We apply a random or regular pattern with good contrast to the surface of the test object. The initial imaging processing defines unique correlation areas, known as facets, across the entire imaging area and that typically range in size from 5 to 20 square pixels.
2. Data acquisition and processing: An image correlation algorithm tracks the movement of these facets by utilizing mathematical methods to maximize the similarity measures from successive images. We can then calculate the three-dimensional locations of each facet and obtain full-field displacement data by tracking these measurement facet points within the applied random (or regular) target pattern.
3. Results: When measurements are taken, they give us an out-of-plane displacement (or deformation) map for the entire surface for each point in time. Calculations using the displacement maps at different times during the testing period or long-term operation show the progression of expansion or relaxation of structure affected by various degradation mechanisms, including the ASR.

As part of the inter-pathway collaboration within the Light Water Research Sustainability Program, Vanderbilt University is conducting research to investigate the monitoring of degradation in concrete sample at the University of Tennessee - Knoxville due to ASR using the DIC technique. A black-background-white-speckle pattern using acrylic latex paint was selected and applied to the slab. At the same time, the supporting fixtures for the DIC camera were also installed inside the environmental chamber. The technical basis for selecting optimal experimental settings were discussed in the Neal et al. (2016).

6.2 DIC Results

The results for the DIC strain calculations are shown in Table 6, along with the date the tests were conducted and other variables. Figure 43 shows the plot for the average strains calculated using DIC in the X and Y directions over time. There is a large spike in the stain in both the X and Y directions during the month of February 2017. There is also an increase in June 2018 when the temperature of the slab was increased to try and further expansion. The strain then decreases in August 2018 when the temperature was lowered again.

Table 6: DIC measurements taken bimonthly on the slab.

Date	Time of Meas.	Stage	Average Δεx (μm/m)	Average Δεy (μm/m)	Facets	Facet % Loss	T (°C) Slab
8/18/2016	1-2pm	0	---	---	15021	0	28.4183
10/17/2016	9-11am	11	1320	1090	14699	-2.14	38.2511
12/12/2016	9-11am	26	Bad Data	Bad Data	---	---	37.8926
2/17/2017	9-11am	31	2240	1930	14644	-2.51	36.7511
4/22/2017	9-11am	36	1780	1610	14545	-3.17	33.099
6/28/2017	9-11am	46	1750	1580	14683	-2.25*	37.8002
8/24/2017	9-11am	66	1700	1510	14706	-2.10**	23.9259
10/19/2017	9-11am	76	1620	1430	14532	-3.26	23.9
12/15/2017	9-11am	86	1650	1470	14605	-2.77	23.9
03/21/2018	9-11 am	96	1720	1560	14541	-3.20	23.8
06/27/2018	9-11 am	116	1850	1640	14653	-2.45	31.8
08/16/2018	9-11 am	126	1680	1500	14668	-2.35	24.7

*+1.01% facet gain on 6/28 compared to 4/22 is due to increased LED lighting.
**+.015% facet gain on 8/24 compared to 6/28 is likely due to lighting and/or camera position change.

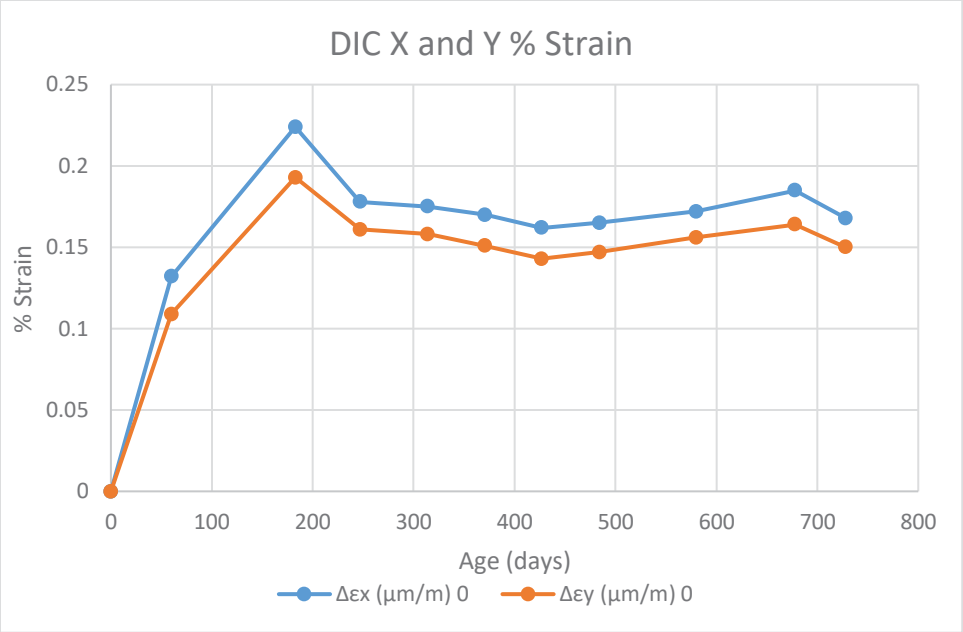

Figure 43: Plot of the average DIC strain in the X and Y directions over time.

7. SUMMARY AND FUTURE WORK

The objectives of this report were to examine the application of VAM and DIC techniques in ASR damage diagnosis and to develop approaches for uncertainty quantification in diagnosis. Researchers applied the VAM technique to a 24 in. x 24 in. x 6 in. slab cast at Vanderbilt University with four pockets of reactive aggregates, and four 24 in. x 12 in. x 12 in. slabs with reactive and non-reactive aggregates (dispersed throughout the slabs). The DIC technique was applied to a large concrete mock-up at the University of Tennessee, Knoxville. The main outcomes of the experiments and subsequent analyses include:

1. VAM successfully detected and localized the damage in the medium-sized concrete slabs from both Vanderbilt and Alabama. The occurrence of sidebands is dependent on the pumping and probing actuator locations, the two excitation amplitudes, and the two excitation frequencies.
2. The uncertainty quantification effort first developed a neural network surrogate model to speed up the forward and inverse problems in uncertainty quantification.
3. The neural network model is verified by comparison with the experimental data, and the agreement is observed to be moderate.
4. The neural network model is employed to quantify the uncertainty in the damage diagnosis, showing the result as probability of damage at each location.
5. The neural network is also employed for sensitivity analysis, thus quantifying the relative contributions of different experimental parameters on the uncertainty of the damage diagnosis.
6. The monitoring of the large specimen at the University of Tennessee is complete, and the DIC analysis results presented in this report cover the entire range of DIC data collected over the two-year period.

Future work needs to focus on the following issues:

1. The VAM technique has generally shown good performance in terms of identifying the damage locations. Future work needs to focus on scaling up the technique to large-scale, field implementation of VAM-based diagnosis in NPP concrete structures. One of the key challenges is the number of sensors (accelerometers) needed. For a large structure, it is not feasible to use a large number of accelerometers. It might be beneficial to instead use a remote-sensing full-field observation technique (such as laser vibrometry).
2. Scaling up VAM to realistic applications also requires the combination of computational modeling with experiments to further improve the damage localization. A related issue is the effect of uncertainty in diagnosis and prognosis, due to sensor noise, model uncertainty, and many other sources of concrete variability.
3. The uncertainty quantification methodology presented in this report was applied to VAM-based diagnosis and prognosis. However, the methodology is general, and is capable of being applied to multiple technique that collect spatially distributed data. Future work needs to investigate the incorporation of uncertainty quantification in developing a robust Prognostics and Health Management (PHM) framework.

8. REFERENCES

Agarwal, V. and S. Mahadevan, 2014, "Concrete Structural Health Monitoring in Nuclear Power Plants," *Office of Nuclear Energy Sensors and Instrumentation Newsletter*, September 2014.

ASTM C1293-08b, 2015, "Standard Test Method for Determination of Length Change of Concrete due to Alkali-Silica Reaction," ASTM International, August 2015.

ASTM C1567-13, 2013, "Standard Test Method for Determining the Potential Alkali-Silica Reactivity of Combinations of Cementitious Materials and Aggregate (Accelerated Mortar-Bar Method)," ASTM International, 2013.

Bruck, P., T. Esselman, and M. Fallin, 2012, "Digital Image Correlation for Nuclear," *Nuclear Engineering International*, April 23, 2012.

Chen, J., A. R. Jayapalan, J.-Y. Kim, K. E. Kurtis, and L. J. Jacobs, 2009, "Nonlinear wave modulation spectroscopy method for ultra-accelerated alkali-silica reaction assessment," *ACI Materials Journal*, Vol. 106, pp. 340–348.

Chen, X. J., J.-Y. Kim, K. E. Kurtis, J. Qu, C. W. Shen, and L. J. Jacobs, 2008, "Characterization of progressive microcracking in Portland cement mortar using nonlinear ultrasonics," *NDT&E International*, Vol. 41, pp. 112–118.

Christensen, J. A., 1990, "NPAR Approach to Controlling Aging in Nuclear Power Plants," *Proceedings of the 17th Water Reactor Safety Information Meeting*, Washington, D.C., NUREG/CP-0105, Vol. 3, pp. 509–529.

Kim, S., D. E. Adams, H., Sohn, G. Rodriguez-Rivera, N. Myrent, R. Bond, J. Vitek, S. Carr, A. Grama, and J. J. Meyer, 2014, "Crack detection technique for operating wind turbine blades using Vibro-Acoustic Modulation," *Structural Health Monitoring*, Vol. 13, No. 6, pp. 660–670.

Kreitman, K., 2011, "Nondestructive Evaluation of Reinforced Concrete Structures Affected by Alkali-Silica Reaction and Delayed Ettringite Formation," M.S. Thesis: University of Texas at Austin, Austin, Texas.

Lapedes, A. S., & Farber, R. M. (1988). How neural nets work. In *Neural information processing systems* (pp. 442-456).

Mahadevan, S., V. Agarwal, K. Neal, D. Kosson, and D. Adams, 2014, *Interim Report on Concrete Degradation Mechanisms and Online Monitoring Techniques*, INL/EXT-14-33134, Idaho National Laboratory, September 2014.

Mahadevan, S., V. Agarwal, K. Neal, P. Nath, Y. Bao, G. Cai, P. Orme, D. Adams, and D. Kosson, 2016, *A Demonstration of Concrete Structural Health Monitoring Framework for Degradation due to Alkali-Silica Reaction*, INL/EXT-16-38602, Idaho National Laboratory, April 2016.

Mahadevan, S., S. Miele, K. Neal, Y. Bao, V. Agarwal, B. T. Pham, D. Adams, and D. Kosson, 2017, *Interrogation of Alkali-Silica Reaction Degraded Concrete Samples using Acoustic and Thermal Techniques to Support Development of a Structural Health Monitoring Framework*, INL/EXT-17-41852, Idaho National Laboratory, April 2017.

Mahadevan, S., S. Miele, P. Karve, J. Frinfrock, V. Agarwal, E. Giannini, 2018, *Enhancement of the Structural Health Monitoring Framework by Optimizing Vibro-Acoustic Modulation Techniques to Localize Alkali-Silica Reaction Degradation in Medium-Sized Concrete Samples*, INL/EXT-18-45212, Idaho National Laboratory, April 2018.

Naus, D., 2007, "Activities in Support of Continuing the Service of Nuclear Power Plant Safety-Related Concrete Structures," in *Infrastructure Systems for Nuclear Energy,* T. T. C. Hsu, C.-L. Wu, and J.-L. Li (eds), Chichester, United Kingdom: John Wiley & Sons, Ltd.

Neal, K., S. Mahadevan, V. Agarwal, G. Thorne, D. Koester, and B. T. Pham, 2016, *Digital Image Correlation of Concrete Slab at University of Tennessee, Knoxville*, INL/EXT-16-39921, Idaho National Laboratory, September 2016.

NextEra Energy Seabrook, 2012, "Impact of Alkali-Silica Reaction on Concrete Structures and Attachments," the Response to Confirmatory Action Letter, SBK-L-12106, from NextEra Energy Seabrook to the Nuclear Regulatory Commission (NRC), May 24, 2012.

Nuttall, Albert H. "Some Windows with Very Good Sidelobe Behavior." IEEE Transactions on Acoustics, Speech, and Signal Processing. Vol. ASSP-29, February 1981, pp. 84–91.

Singh, A. K., Chen, B., Tan, V. B., Tay, T. E., & Lee, H. P. ,2017. A theoretical and numerical study on the mechanics of vibro-acoustic modulation. The Journal of the Acoustical Society of America, 141(4), 2821-2831

Sobol, I.M. "Global sensitivity indices for nonlinear mathematical models and their Monte Carlo estimates," Mathematics and Computers in Simulation, Vol. 55, No. 1–3, pp. 271–280, 2001.

Ulm, F. J., O. Coussy, L. Kefei, and C. Larive, 2000, "Thermo-chemo-mechanics of ASR expansion in concrete structures," *Journal of Engineering Mechanics*, Vol. 126, No. 3, pp. 233–242.

Welch, P. D. (1967), "The use of Fast Fourier Transform for the estimation of power spectra: A method based on time averaging over short, modified periodograms", IEEE Transactions on Audio and Electroacoustics, AU-15 (2): 70–73